Michael Pusterhofer, BSc

# Atom-surface interaction of topological insulators determined by close-coupling calculations and helium atom scattering measurements

**Master's thesis**

to achieve the university degree of

Diplom-Ingenieur

Master's degree programme: Technische Physik

submitted to

**Graz University of Technology**

Supervisor

Univ.-Prof. Dipl-Phys. Dr.rer.nat. Wolfgang E. Ernst

Co-advisor

Dr. Anton Tamtögl

Institute for Experimental Physics
Head: Univ.-Prof. Dipl-Phys. Dr.rer.nat. Wolfgang E. Ernst

Graz, September 2017

## Affidavit

I declare that I have authored this thesis independently, that I have not used other than the declared sources/resources, and that I have explicitly indicated all material which has been quoted either literally or by content from the sources used. The text document uploaded to TUGRAZonline is identical to the present master's thesis.

Graz, _____ _____

Date Signature

## Eidesstattliche Erklärung

Ich erkläre an Eides statt, dass ich die vorliegende Arbeit selbstständig verfasst, andere als die angegebenen Quellen/Hilfsmittel nicht benutzt, und die den benutzten Quellen wörtlich und inhaltlich entnommenen Stellen als solche kenntlich gemacht habe. Das in TUGRAZonline hochgeladene Textdokument ist mit der vorliegenden Masterarbeit identisch.

Graz, am _____ _____

Datum Unterschrift

# Abstract

In the course of this master's thesis the atom-surface interaction of the topological insulator $Bi_2Te_3$ is investigated using helium atom scattering. The focus of this work is the determination of the interaction potential between the helium atom and the sample surface, which can be achieved by analysing experimental measurements with the assistance of quantum mechanical simulations. Since the research field of topological insulators is relatively young, little experimental data, that enables the determination of the interaction potential, is available. Using the angle/energy resolved helium atom scattering intensity in the background signal as well as the intensity ratio between the elastic peaks, insights into the nature of the surface potential is gained. By applying an elastic close-coupling simulation, which can reproduce the measurements, the potential parameters can be optimized by comparing experimental and simulated features. Using the selective adsorption signals from the scattering spectra of the $Bi_2Te_3(111)$ surface an averaged potential was identified, which could be extended to a three-dimensional potential using further measurements and simulations. To improve on these results a parameter study was conducted to reduce the uncertainty of the potential parameters. This leads the way for more precise simulations, which incorporate inelastic effects to generate insights into the lifetime of bound states as well as the electron-phonon coupling.

# Kurzfassung

Im Rahmen dieser Masterarbeit wird die Atom-Oberflächen-Wechselwirkung am topologischen Isolator $Bi_2Te_3$ mittels Heliumstreuung untersucht. Dabei liegt der Fokus auf der Bestimmung des Wechselwirkungspotentials zwischen dem Heliumatom und der Oberfläche, welches durch die Auswertung von experimentellen Messungen, unter der Zuhilfenahme von quantenmechanischen Simulationen, bestimmt werden kann. Da das Forschungsgebiet der topologischen Isolatoren noch relativ jung ist, existieren kaum experimentelle Daten, die eine Ermittlung des Wechselwirkungspotentials zulassen. Jedoch lassen sich mittels winkel- und energieaufgelöster Heliumstreuung Intensitätsschwankungen im Hintergrundstreusignal, sowie das Intensitätsverhältnis der elastischen Streupeaks nutzen, um Einblicke in die Beschaffenheit des Oberflächenpotentials zu erlangen. Durch die Kombination mit einer elastischen Close-Coupling-Simulation, welche diese Messungen reproduzieren kann, können die Potentialparameter durch das Vergleichen von experimentellen und simulierten Features optimiert werden. Dazu wurden selektive Adsorptionssignale aus den Streuspektren der $Bi_2Te_3(111)$ Oberfläche genutzt, um ein mittleres Potential zu bestimmen, das mithilfe weiterer Messungen und unter Verwendung von Simulationen in ein dreidimensionales Potential überführt werden kann. Um dieses Ergebnis noch zu verbessern wurde zudem eine Parameterstudie durchgeführt, die die Potentialparameter weiter einengen konnte. Dadurch wird die Verwendung des Potentials in weiterführenden Simulationen möglich, die durch das Miteinbeziehen von inelastischen Effekten Einblicke in die Lebensdauer der gebundenen Zustände sowie die Elektron-Phonon Kopplung geben können.

# Contents

# List of Figures

# 1. Introduction

Helium Atom Scattering (HAS) is an important tool for investigating material surfaces, which is complementary to other diffraction techniques like electron scattering or low energy electron diffraction (LEED), electron energy loss spectroscopy (EELS), as well as neutron scattering. It is well known that electrons and neutrons penetrate several layers into the crystal, whereas helium atoms are reflected by even a very weak surface electron density. Thus HAS is the only method which is sensitive to the outermost layer and is non-destructive as the helium atom is not charged and does not produce any radiation damage. The electrical neutral property of the helium atom is also useful for investigating charged surfaces, which can be found on insulators and semiconductors [1].

Using HAS the surface phonon dispersion, structural properties, as well as the surface interaction potential can be investigated.

He atom scattering offers the prospect of detailed insights into the nature of atom-surface interactions. The main aim of this study is to achieve an in-depth understanding of the atom-surface interaction on the newly discovered class of topological insulators. In the course of this work, the Helium-Bismuth Telluride interaction potential was investigated. Topological insulator surfaces typically feature an unusual combination of metallic surface states together with a strongly corrugated surface electron density. A better understanding of scattering from these surfaces would enable new insights into the nature of strongly corrugated surface potentials, where overlapping and interacting resonances are common. One of these processes used in the analysis is the selective adsorption resonance (SAR). By analysing those resonances, using results obtained by HAS, in combination with quantum mechanical simulations, information about the surface potential is gained. To make sure the correct values for the potential parameters are obtained, two methods of optimisation are used. One looks at the SAR found in the measurements from a kinematic

point of view and the other one tries to find the best matching quantum mechanical simulation by applying a $\chi^2$-test to the simulated SAR positions calculated for different parameter sets.

At the beginning of this thesis, the theoretical background of the used concepts is discussed to provide the basic understanding needed for later chapters. The material investigated also has its own little chapter explaining some of its properties and after Chapter 4, where the experimental measurements are discussed, Chapter 5 can be found, which contains the analysis, which leads to the surface interaction potential. In the last chapter, the results are summarised.

# 2. Theoretical background

In this chapter, an overview of the used theories, processes and definitions is given. This includes some basic concepts like crystals as well more specialised concepts like the close-coupling (CC) algorithm. For more details on the specific topics, the reader is referred to the literature as this summarises just the relevant parts.

## 2.1. Crystals

Crystals are materials, that possess simple periodic structures. Their atom positions can be described as a set of locations replicated on a periodic grid. For three dimensions these grids can be categorised into 14 different types, which are called Bravais lattices. To describe the lattice, each point $r$ is represented by a set of 3 integer numbers $u_1$,$u_2$,$u_3$, scaling the 3 primitive vectors $\mathbf{a}_1$, $\mathbf{a}_2$, $\mathbf{a}_3$ as seen in equation 2.1

$$\mathbf{r} = u_1\mathbf{a}_1 + u_2\mathbf{a}_2 + u_3\mathbf{a}_3 \tag{2.1}$$

The investigation of surfaces is an interesting research topic, because there the crystal symmetry and the chemical equilibrium is broken. To describe the different surfaces of a crystal, the Miller-Indices can be used. These indices are composed of three integers written as the triple (hkl) and describe a plane that intersects the points $\mathbf{a}_1/h$, $\mathbf{a}_2/k$ and $\mathbf{a}_3/l$.

To describe points on a two-dimensional surface only two surface vectors $\mathbf{A}_1$ and $\mathbf{A}_2$ and the numbers $c_1$ and $c_2$ are needed. This works equivalent to the three-dimensional case and can be seen in equation 2.2 adopting the nomenclature of Cabrera *et. al.* [2], where vectors on the surface are written as capital letters.

$$\mathbf{R} = c_1\mathbf{A}_1 + c_2\mathbf{A}_2 \tag{2.2}$$

Another important concept to describe a crystal is the reciprocal lattice. It can be obtained by Fourier transformation of the lattice described before. For a three-dimensional lattice, this leads to a set of equations using the reciprocal basis vectors $\mathbf{b}_i$ [3]:

$$\mathbf{b}_1 = 2\pi\frac{\mathbf{a}_2 \times \mathbf{a}_3}{\mathbf{a}_1 \cdot (\mathbf{a}_2 \times \mathbf{a}_3)}; \quad \mathbf{b}_2 = 2\pi\frac{\mathbf{a}_3 \times \mathbf{a}_1}{\mathbf{a}_1 \cdot (\mathbf{a}_2 \times \mathbf{a}_3)}; \quad \mathbf{b}_3 = 2\pi\frac{\mathbf{a}_1 \times \mathbf{a}_2}{\mathbf{a}_1 \cdot (\mathbf{a}_2 \times \mathbf{a}_3)} \tag{2.3}$$

The two-dimensional basis can be obtained by extending the basis vectors $\mathbf{A}_i$ to the third dimensions using the normalised basis vector in the $\mathbf{a}_3$-direction as the third basis vector. This leads to three reciprocal basis vectors, where $\mathbf{b}_1$ is used as $\mathbf{B}_1$,$\mathbf{b}_2$ corresponds to $\mathbf{B}_2$, and $\mathbf{b}_3$ is discarded. Knowing the reciprocal basis vectors, the reciprocal vector $\mathbf{g}$ can then be written as

$$\mathbf{g} = v_1\mathbf{b_1} + v_2\mathbf{b_2} + v_3\mathbf{b_3} \qquad v_1, v_2, v_3 \in \mathbb{Z}, \tag{2.4}$$

which, for the two-dimensional case, changes to

$$\mathbf{G} = d_1\mathbf{B_1} + d_2\mathbf{B_2} \qquad d_1, d_2 \in \mathbb{Z}. \tag{2.5}$$

In the case of a hexagonal lattice given by equation 2.7, the reciprocal lattice is another hexagonal lattice, which is rotated by 60° with respect to the original lattice. This is shown in figure 2.1 and can be calculated using

$$\mathbf{B}_1 = \frac{2\pi}{\sqrt{3}a}\left(\sqrt{3}\mathbf{K}_x + \mathbf{K}_y\right) \quad \mathbf{B}_2 = \frac{4\pi}{\sqrt{3}a}\left(\mathbf{K}_y\right), \tag{2.6}$$

when the hexagonal lattice is given by equation 2.7 using $a$ as the lattice constant.

$$\mathbf{A_1} = a\mathbf{X} \quad \mathbf{A_2} = -\frac{a}{2}\mathbf{X} + \frac{\sqrt{3}a}{2}\mathbf{Y}, \tag{2.7}$$

## 2.2. Helium atom scattering

Atom scattering is a method to investigate structures and dynamics of surfaces. Unlike X-ray scattering or neutron scattering, the atom scattering method can be used to measure only the surface interactions, whereas neutrons and X-rays penetrate into the bulk. Using uncharged helium the effect of surface charges can be minimised. This makes

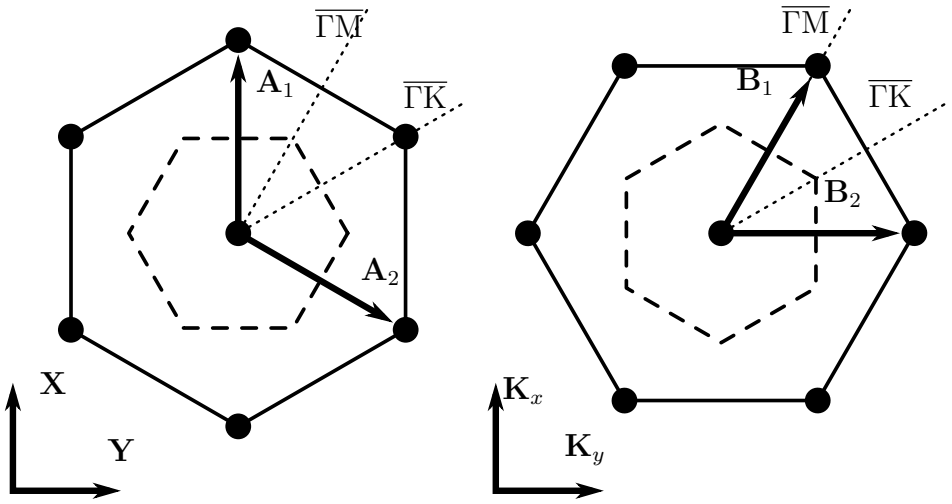


Figure 2.1.: Real(left) and reciprocal space(right) for a simple hexagonal lattice: The left-hand side shows the real-space lattice with its Wigner-Seitz-cell(dashed hexagon) and the right-hand side shows the corresponding reciprocal lattice as well as its first Brillouin zone(dashed hexagon). The used real-space basis is given by $\mathbf{X}$ and $\mathbf{Y}$ and for the reciprocal space, the basis consists of $\mathbf{K}_X$ and $\mathbf{K}_Y$. In addition to the lattice, dashed lines are displayed, which represent the $\overline{\Gamma M}$- and $\overline{\Gamma K}$- directions used in the measurements.

it possible to investigate samples which tend to build surface charges, such as insulators and semiconductors. In addition, helium has no electric charge and is nonreactive, which avoids chemical interactions with the surface.

When analysing helium surface interactions, elastic and inelastic scattering can be observed as well as surface adsorption resonances. For this work however, the inelastic scattering interactions are not of particular interest and will not be discussed. Information about inelastic effects on helium can be found in [4].

### 2.2.1. Elastic scattering

Elastic scattering conserves energy and can be observed if the helium beam has a wavelength similar to the lattice constant. To calculate the positions of the scattering peaks the Laue condition can be used, which states that the scattering vector $\Delta\mathbf{k}$ must

be equal to a reciprocal lattice vector $\mathbf{g}$:

$$\Delta\mathbf{k} = \mathbf{k}_f - \mathbf{k}_i = \mathbf{g} \tag{2.8}$$

The incoming wave vector $\mathbf{k}_i$ and the outgoing wave vector $\mathbf{k}_f$ can be used to get the scattering vector, but on a two-dimensional lattice, equation 2.8 is reduced to

$$\Delta\mathbf{K} = \mathbf{K}_f - \mathbf{K}_i = \mathbf{G}, \tag{2.9}$$

where only the component parallel to the surface of the wave vectors $\mathbf{K}_f$ and $\mathbf{K}_i$ are used. To make this scattering process elastic the process also has to conserve energy. This can be expressed as

$$|\mathbf{k}_i| = |\mathbf{k}_f|\,, \tag{2.10}$$

because the beam energy is proportional to $\mathbf{k}^2$. Combining equation 2.9 and 2.10 the scattering peaks are uniquely defined. In the case of an apparatus with a fixed source-detector angle $\theta_{SD} = \theta_i + \theta_f$ the scattering vector can be written as

$$\Delta K(\theta_i) = |\mathbf{k_i}|\,(\sin(\theta_f) - \sin(\theta_i)) = 2\,|\mathbf{k_i}|\cos\left(\frac{\theta_{SD}}{2}\right)\sin\left(\frac{\theta_{SD}}{2} - \theta_i\right), \tag{2.11}$$

which, when combined with equation 2.9, can be rearranged to calculate the incident angle $\theta_i$ at which a peak should occur:

$$\theta_i = \frac{\theta_{SD}}{2} - \arcsin\left(\frac{G}{2k_i\cos\left(\frac{\theta_{SD}}{2}\right)}\right) \tag{2.12}$$

### 2.2.2. Selective adsorption resonances

Selective adsorption was first explained by J.E.Lennard-Jones and A.F.Devonshire [5] when I.Estermann, R.Frisch and O.Stern observed unexpected weakening of scattered intensity at certain beam energies, investigating LiF [6]. They explained it by purely kinematic means, where the atom can move freely along the surface but experiences an oscillatory or bound motion perpendicular to the surface. Eventually the bound atom is lost, due to inelastic scattering or energy loss to the solid, which explains the found minima. This explanation is largely correct, but the part which described the outcome of

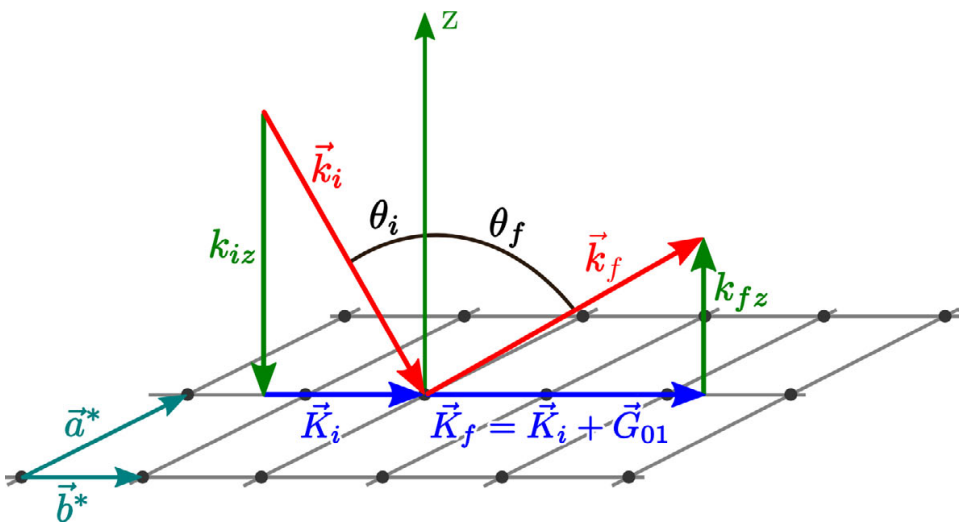


Figure 2.2.: Surface scattering geometry: The wave vector corresponding to the incident beam $\mathbf{k}_i$ and the wave vector of the outgoing beam $\mathbf{k}_f$, as well as their components, are shown on the reciprocal lattice. If the difference between $\mathbf{K}_i$ and $\mathbf{K}_f$ is equal to a reciprocal lattice vector $\mathbf{G}$, elastic peaks can be observed [4].

the bound atom is incorrect. It was pointed out that the reverse process of emitting a surface bound atom, should also be possible [5]. In this process the bound atom stays at the surface for some time (typically of the order of $10^{-10}$ s [7] or $10^{-11}$ s [8]) and leaves the surface as an outgoing beam. This causes interferences with the scattered beam, which leads to peaks or dips in the intensity [9]. Those peaks can have different line shapes ranging from Lorentzian minima and maxima to Fano-type profiles [10].

The following formulae are written in natural units, where $\frac{\hbar^2}{2m} = 1$, using the helium mass $m$. The incidence condition for a SAR can be written as

$$\mathbf{k}_{\mathbf{B},z}^2 = \mathbf{k}_i^2 - (\mathbf{K}_i + \mathbf{B})^2 = -|\epsilon_n|\,, \tag{2.13}$$

where the z-component of the wave vector after a scattering process with the scattering vector $\mathbf{B}$ has to be equal to the n-th negative bound state energy $\epsilon_n$ of the surface averaged interaction potential $V_0$. This can only happen if the scattering vector $\mathbf{B}$ corresponds to a closed channel as the definition of a closed channels is $\mathbf{k}_{\mathbf{B},z}^2 < 0$ [10].

A common notation for SARs consists of three integer values to define the scattering vector, which defines the resonant channel and the level of the used bound state. This

can be written as $\binom{d_1\ d_2}{n}$ which describes a resonance using the scattering vector $\mathbf{B} = d_1\mathbf{B_1} + d_2\mathbf{B_2}$ and the n-th bound state from the surface averaged potential $V_0$. This is useful if $V_0$ is already known, but when analysing resonances it is also useful to provide the bound state energy $\epsilon$ in milli-electron volts. This is done by writing $\binom{d_1\ d_2}{\epsilon}$, where the energy is given as a floating point number instead of an integer.

## 2.3. Experimental setup

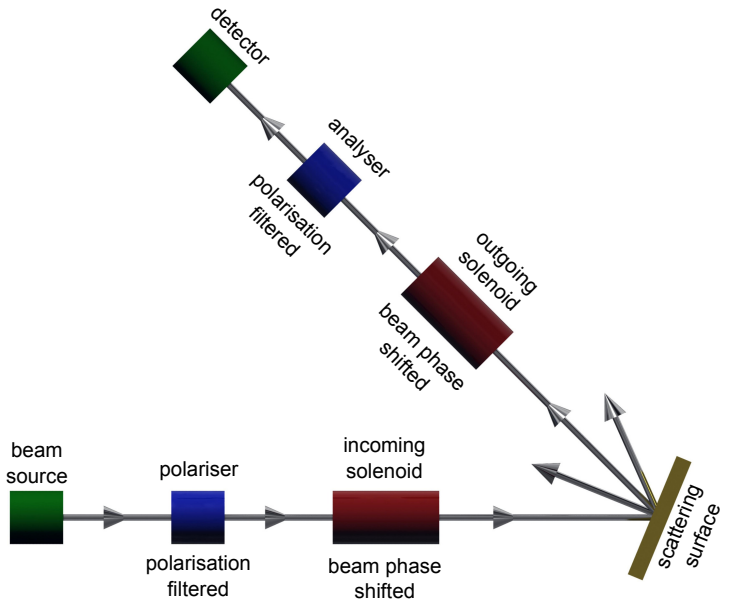


Figure 2.3.: Outline of the Cambridge spin-echo apparatus: An unpolarised beam of thermal $^3$He is generated from the source in a fixed direction. The nuclear spins are polarized and then rotated by the incoming (initial) solenoid before being scattering upon the target crystal surface. Afterwards any scattered $^3$He atoms heading in the direction of the detector passes through the the outgoing (final) solenoid,which rotates the spin again, and through another polarisation filter before being detected.

The $^3$He spin-echo apparatus is based on the same principle as neutron spin-echo spectrometers. However, instead of neutrons, which penetrate into the bulk, $^3$He is used. The repulsive part of the $^3$He/surface interaction potential prevents the He atoms from penetrating into the surface layer of materials. Consequently, they are an ideal surface scattering probe that allows to truly understand surface processes [11].

A schematic drawing of the Cambridge spin-echo apparatus is shown in figure 2.3. First an unpolarized $^3$He beam is created by supersonic expansion from the source. Since $^3$He exhibits an overall spin of one-half, a strong magnetic field can be used to polarise the beam. The polarised beam then passes through a solenoid field which gives rise to a precession of the spin around the beam axis, which depends on the time spent in the magnetic field.

If the apparatus is used to measure dynamic surface effects, the beam is created with a very narrow energy bandwidth. After scattering, the beam passes through the second solenoid, which reverses the spin precession introduced in the first one. If the sample is static the original beam is recovered, but if the sample changes and energy is transfered to the beam, the precession cannot be undone. This leads to a lower signal after the analyser is passed and the intensity is measured.

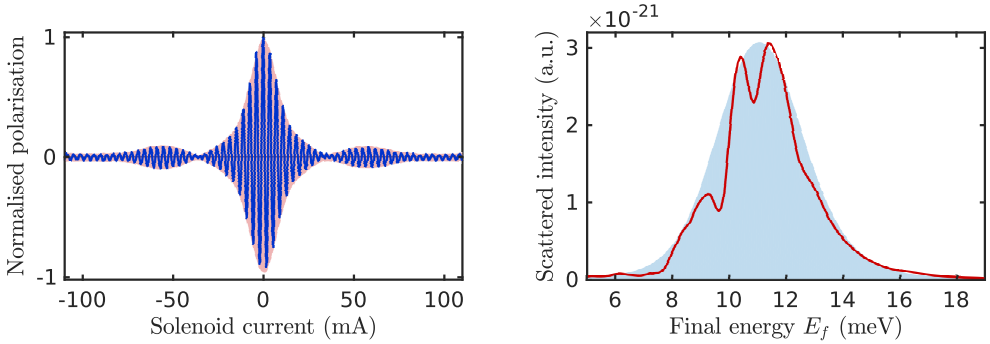


Figure 2.4.: Raw and processed HAS signal: On the left-hand side, the detector signal for different currents in the first solenoid can be seen. The current is proportional to the magnetic field, which changes the polarisation of the polarised helium beam. The overall decay envelope is due to the (velocity) energy spread of the beam. The beating effect is an interference pattern due to the existence of multiple energy (velocity) peaks within the overall beam energy distribution. These multiple energy peaks are a result of SARs. After transforming the signal to an energy scale, which is done by a Fourier transformation, resonances can be seen in the energy distribution (right side). The blue background shows the helium beam profile before the scattering process.

When measuring SARs, the second solenoid current is set to 0 mA and the beam is created with a broader energy bandwidth. After polarisation, the beam also passes through the first solenoid with a defined current and scatters off the target. As only a part of the scattered beam passes through the analyser and the detector, the measurement is often

taking place at the specular peak position to optimise the signal to noise ratio. By changing the current in the first solenoid and measuring the detector current, the solenoid current can be transformed to an energy scale using Fourier transformation. This is shown in figure 2.4. By varying the azimuth angle $\phi$, a two-dimensional signal distribution can be created.

## 2.4. Close-coupling simulation

To determine some properties of a sample, which are difficult to measure directly, an indirect method can be used. In many cases, this indirect method involves a simulation, which tries to predict a certain behaviour of the sample for a given set of material properties. One example are the elastic peak heights, which can be verified by comparison with the measured data.

If the simulation is good enough it is possible to search sets of parameters which reproduce the measured data. For an atom scattering process like helium scattering, one method for doing so is the close-coupling method. To keep the following formulas compact they are given in natural units as in chapter 2.2.2.

Starting point is the time independent Schrödinger equation, which for the scattering process can be written as:

$$\left[-\nabla^2 + V(\mathbf{r}) - {\mathbf{k}_i}^2\right] \psi(\mathbf{r}) = 0, \tag{2.14}$$

Here the wave function $\psi$, the incident wave vector $\mathbf{k}_i$ and the potential $V$ are used. The potential exhibits the periodicity of the surface lattice and can be written as a Fourier series.

$$V(\mathbf{r}) = \sum_{\mathbf{G}} V_{\mathbf{G}}(z) \exp(i\mathbf{G} \cdot \mathbf{R}) \tag{2.15}$$

Analogously, wave function $\psi$ can be rewritten:

$$\psi(\mathbf{r}) = \sum_{\mathbf{G}} \psi_{\mathbf{G}}(z) \exp(i(\mathbf{G} + \mathbf{K}_i) \cdot \mathbf{R}) \tag{2.16}$$

Inserting the latter two equations into equation 2.14. leads to:

$$\left[\frac{d^2}{dz^2} + \mathbf{k}^2{}_{\mathbf{G},z} - V_0(z)\right]\psi_{\mathbf{G}}(z) = \sum_{\mathbf{G}'\neq\mathbf{G}} V_{\mathbf{G}-\mathbf{G}'}(z)\psi_{\mathbf{G}'}(z) \tag{2.17}$$

for the z-direction, where $\mathbf{k}^2_{\mathbf{G},z}$ is the z-component of the particles kinetic energy after the surface interaction and $V_0$ is the surface-averaged interaction potential:

$$\mathbf{k}^2_{\mathbf{G},z} = \mathbf{k}_i^2 - (\mathbf{K}_i + \mathbf{G})^2 \tag{2.18}$$

To solve equation 2.17 the Fox-Goodwin method can be used. This method has the advantage of being very stable in the asymptotic region, where the wave function is almost static. The first step in this method is to rearrange equation 2.17 using $V_0 = V_{\mathbf{G}-\mathbf{G}'}$ if $\mathbf{G} - \mathbf{G}' = 0$:

$$\frac{d^2}{dz^2}\psi_{\mathbf{G}}(z) = \sum_{\mathbf{G}'}\left[-\delta_{\mathbf{G},\mathbf{G}'}\mathbf{k}^2_{\mathbf{G}',z} + V_{\mathbf{G}-\mathbf{G}'}(z)\right]\psi_{\mathbf{G}'}(z) \tag{2.19}$$

This form makes it possible to bring the system of equations into a matrix-form, because the close-coupling method treats every $\psi_{\mathbf{G}}$ as a scattering channel. The channels are divided into open and closed channels, where open channels exhibit a kinetic energy in the z-component $k^2_{G,z} > 0$ and the closed channels have negative kinetic energy $k^2_{G,z} < 0$. Using this, the matrix equation is created in a way that $\mathcal{F}$ represents a matrix, where every column is a set of equations with a different excited channel. Therefore, there are as many rows as channels and columns as open channels, because only an open channel can be excited. $\mathcal{W}$ represents the coupling between each of those channels. With all these elements the matrix equation can be written as

$$\frac{d^2}{dz^2}\mathcal{F}(z) = \mathcal{W}(z)\mathcal{F}(z), \tag{2.20}$$

which can be solved using a Numerov algorithm. This algorithm discretizes the equation as seen in equation 2.21, to find a solution by taking small steps from an initial point.

$$\left[\mathbb{1} - \frac{\hbar^2\mathcal{W}_{i+1}}{12}\right]\mathcal{F}_{i+1} + \left[\mathbb{1} - \frac{\hbar^2\mathcal{W}_{i-1}}{12}\right]\mathcal{F}_{i-1} - \left[\mathbb{1} + \frac{10\hbar^2\mathcal{W}_i}{12}\right]\mathcal{F}_i = 0 \tag{2.21}$$

One disadvantage of the Numerov algorithm is that it can be very unstable in the asymptotic region. To avoid this the wave function is not solved directly, instead a propagation matrix $\mathcal{R}$ is solved as described in the Fox-Goodwin algorithm.

$$\mathcal{F}_{i-1} = \mathcal{R}_{i-1}\mathcal{F}_i \tag{2.22}$$

Using equation 2.21 and 2.22 the propagation matrix can be expressed as a function of the previous $\mathcal{R}$ matrix, which can be solved by starting with an initial $\mathcal{R}_0$ matrix. This initial matrix is assumed to be zero for all its elements.

$$\mathcal{R}_i = \left[\left[2\mathbb{1} + \frac{10\hbar^2\mathcal{W}_i}{12}\right] - \left[\mathbb{1} - \frac{\hbar^2\mathcal{W}_{i-1}}{12}\right]\mathcal{R}_{i-1}\right]^{-1} \cdot \left[\mathbb{1} - \frac{\hbar^2\mathcal{W}_{i+1}}{12}\right] \tag{2.23}$$

In the asymptotic region $z \to \infty$ the wave function matrix $\mathcal{F}$ can be written as

$$\mathcal{F} = \begin{pmatrix} \mathcal{S}in \\ 0 \end{pmatrix} + \begin{pmatrix} \mathcal{C}os & 0 \\ 0 & \mathcal{E}xp \end{pmatrix} \cdot \begin{pmatrix} \mathcal{K} \\ \mathcal{E} \end{pmatrix}, \tag{2.24}$$

where $\mathcal{K}$ is the reaction matrix and $\mathcal{E}$ is a coefficient matrix for the closed channels. The initially excited channel, which represents the impinging wave, is described by

$$\mathcal{S}in_{\mathbf{G},\mathbf{G}'} = \frac{\sin(k_{\mathbf{G},z}z)}{\sqrt{k_{\mathbf{G},z}}}\delta_{\mathbf{G},\mathbf{G}'} \tag{2.25}$$

and the backscattered waves are represented by

$$\mathcal{C}os_{\mathbf{G},\mathbf{G}'} = \frac{\cos(k_{\mathbf{G},z}z)}{\sqrt{k_{\mathbf{G},z}}}\delta_{\mathbf{G},\mathbf{G}'} \tag{2.26}$$

The closed channels, which have a decaying nature, are represented by

$$\mathcal{E}xp_{\mathbf{G},\mathbf{G}'} = \frac{e^{-k_{\mathbf{G},z}z}}{\sqrt{k_{\mathbf{G},z}}}\delta_{\mathbf{G},\mathbf{G}'} \tag{2.27}$$

To get the scattering matrix, which contains the scattering probabilities for each channel we need to calculate the reaction matrix $\mathcal{K}$. This can be done by combining Equation 2.22 and Equation 2.24. This results in

$$\left[\mathcal{R}_N \cdot \begin{pmatrix} \mathcal{C}os & 0 \\ 0 & \mathcal{E}xp \end{pmatrix}_N - \begin{pmatrix} \mathcal{C}os & 0 \\ 0 & \mathcal{E}xp \end{pmatrix}_{N-1}\right] \cdot \begin{pmatrix} \mathcal{K} \\ \mathcal{E} \end{pmatrix} = \begin{pmatrix} \mathcal{S}in \\ 0 \end{pmatrix}_{N-1} - \mathcal{R}_N \cdot \begin{pmatrix} \mathcal{S}in \\ 0 \end{pmatrix}_N \tag{2.28}$$

After solving equation 2.28 and extracting the reaction matrix we can use the definition

$$\mathcal{S} = (\mathbb{1} + i\mathcal{K})^{-1}(\mathbb{1} - i\mathcal{K}) \tag{2.29}$$

to calculate the scattering matrix. To get the peak height the part of the scattering matrix where $\mathbf{G} = \binom{0}{0}$ is initially populated is selected, as this is the only part with physical meaning. The calculated square values of $\mathcal{S}$ are then used to represent the peak heights.

## 2.5. Surface potential

The z-component of the interaction potential between the helium atom and the sample surface is composed of an attractive and a repulsive part. The attractive part is present due to Van der Waals forces, whereas the repulsive part emerges from Pauli interactions. In the XY-plane changes of the potential are described by a corrugation function, which is influenced by the surface structure, leading to the same periodicity as seen on the surface.

Based on a comparative study done in 2014, the corrugated Morse potential (CMP) was chosen, because it is easy to use in the computation and produces good results [12]. It is composed of a Morse potential combined with a corrugation function $\xi$ and can be written as

$$V(\mathbf{R}, z) = D\left[\frac{1}{\nu_{0,0}} e^{-2\kappa[z-\xi(\mathbf{R})]} - 2e^{-\kappa z}\right] \tag{2.30}$$

where $\kappa$ is the stiffness parameter, $D$ is the depth of the potential well and $\nu_{0,0}$ is the surface average of the exponent of the corrugation function. In general, $\nu_{\mathbf{G}}$ is defined as

$$\nu_{\mathbf{G}}(z) = \frac{1}{\Sigma}\int_{\Sigma} e^{-i\mathbf{G}\mathbf{R}} e^{2\kappa\xi(\mathbf{R})} d\mathbf{R} \tag{2.31}$$

with $\Sigma$ symbolising the area of the first unit cell. Using a hexagonal unit cell, the corrugation function is created by the summation of cosine terms obtained from a Fourier expansion. By omitting higher orders and introducing a corrugation amplitude $\xi_0$, the corrugation function is given by

$$\xi(\mathbf{R}) = \xi_0\left(\cos\left[\frac{2\pi}{a}(x - \frac{y}{\sqrt{3}})\right] + \cos\left[\frac{2\pi}{a}(x + \frac{y}{\sqrt{3}})\right] + \cos\left[\frac{2\pi}{a}\frac{2y}{\sqrt{3}}\right]\right) \tag{2.32}$$

Thereby, $\nu_{\mathbf{G}}$ can be calculated by a sum of modified Bessel $I$ functions at $\alpha = 2\kappa\xi_0$.

$$\nu_{n,m} = \frac{\sqrt{3}a^2}{4\pi}\sum_k I_k(\alpha)(I_{k+n}(\alpha)I_{k-m}(\alpha) + I_{k-n}(\alpha)I_{k+m}(\alpha)) \tag{2.33}$$

With this, the Fourier coefficients $V_{\mathbf{G}}$ from equation 2.15 can be written as

$$V_{\mathbf{G}}(z) = D\frac{\nu_{\mathbf{G}}}{\nu_{0,0}} e^{-2\kappa z} \tag{2.34}$$

and the averaged surface potential $V_0$ is

$$V_0 = D\left[e^{-2\kappa z} - 2e^{-\kappa z}\right] \tag{2.35}$$

To calculate the potential numerically, the sum over $k$ in equation 2.33 has to be finite. This leads to an approximation, where $k$ is cut off at $|k| \leq k_{co}$. The CC-code also does not use $\xi_0$ as a parameter, instead $h = \frac{3\xi_0}{a}$ is used.

# 3. Topological insulators

A central goal in physics is to characterise phases of matter. Many phases, such as magnets and superconductors can be understood in terms of symmetry considerations. In recent decades phases were discovered which cannot be well characterised by symmetry, such as the quantum Hall effect. This led to the introduction of topological ordering. The research of topological insulators is a relatively new field of study, which emerged from the study of the quantum Hall effect by introducing a strong spin-orbit coupling [13].

The first experimentally realised topological insulator was a quantum well made out of a CdTe/HgTe/CdTe sandwich structure. In 2007, 3D bulk solids of binary compounds containing bismuth were predicted to be topological insulators. Bismuth antimonide was later found to match the prediction, as well as pure antimony, bismuth selenide, bismuth telluride, and antimony telluride [14]. These materials have a band gap in their bulk band structure, but exhibit metallic surface states, which are protected by time-reversal symmetry. These surface states cross each other at a so-called Dirac point and have a linear dispersion. This leads to electrons behaving like massless relativistic particles. Due to the time-reversal symmetry, the surface states are also helical. This means, that their spin orientation and their direction of motion are locked, which suppresses direct backscattering, as the inversion of spins as well as the inversion of the direction of propagation is very unlikely. It increases the mobility of the carriers and makes topological insulators a material for high mobility spintronic applications [15].

## 3.1. Bismuth telluride

One of the bulk topological insulators is bismuth telluride. Its unit cell is composed of three quintuple layers stacked on top of each other. Each quintuple layer consists of

five layers with a stacking sequence of A-B-C-A-B. The material of the layers alternates between bismuth and tellurium where the top layer is made of tellurium. The layers within one quintuple are covalently bonded, whereas the quintuple layers are only weakly bonded by van der Waals forces. This enables the use of the scotch tape method for sample preparation, which uses adhesive tape to peel off a layer of the crystal, exposing only the first layer of the quintuple layer. The surface layer has a hexagonal structure and the distance between the tellurium atoms is about 4.4 Å and the total height of the unit cell is 30.49 Å [15]. From X-ray diffraction measurements a surface atom distance of $(4.373 \pm 0.001)$ Å and a unit cell height of $(30.36 \pm 0.01)$ Å at 100 K was obtained [16].

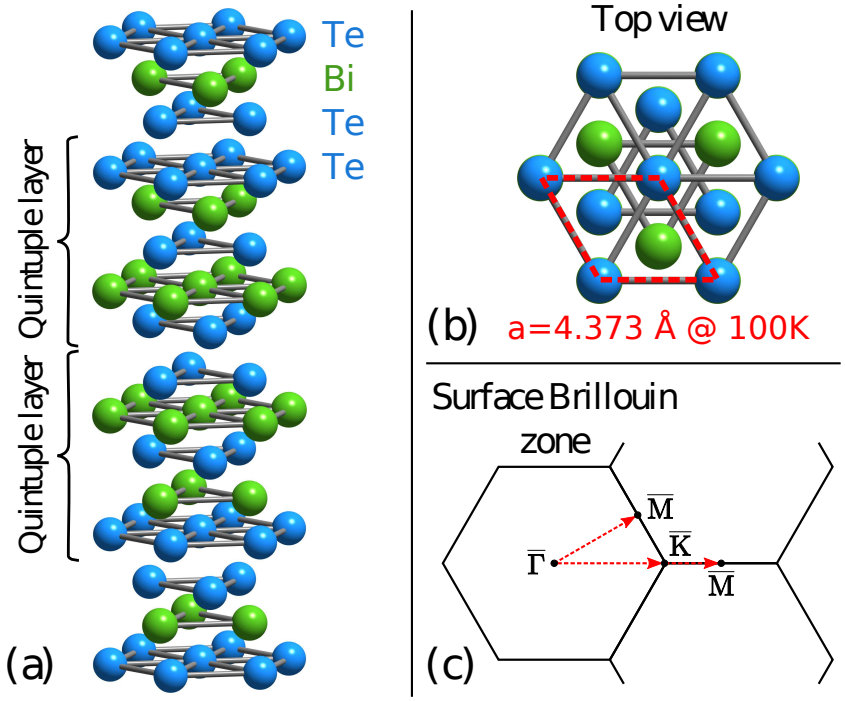


Figure 3.1.: The structure of $Bi_2Te_3$. (a) The stacked quintuple layers, (b) the stacking order of a single layer, (c) Brillouin zone of the surface layer as well as the symmetry points

# 4. Measurements

To investigate the surface of $Bi_2Te_3$, experimental measurements were conducted by Anton Tamtögl in a cooperation between two research groups at the Cavendish Laboratory in Cambridge and the University of Technology in Graz, which enables the investigation of the surface interaction potential. This chapter is about those experimental results, which were obtained by using a $^3$He atom scattering apparatus, as well as the methodology used in the individual measurements.

## 4.1. Sample preparation

As HAS interacts only with the outermost layer of the sample, a clean sample surface is essential to achieve a good signal to noise ratio. One way to achieve this is to cleave the sample in-situ. This removes contaminated parts on the outside of the sample and defines the surface structure, as the cleaving normally occurs along weakly bound crystal planes. $Bi_2Te_3$ can be cleaved in a way that the hexagonal (111)-plane ends up at the surface, because the quintuple layers are weakly bound by van der Waals interactions. This can be seen in Figure 3.1 and enables the use of the scotch-tape method, which is a rather cost-efficient and easy method to use.

The scotch-tape method uses an adhesive tape to remove layers on the outside of the sample by peeling them off with the removal of the tape. This process can be repeated under ambient condition until a good surface is reached. To obtain the final surface the last step is performed in vacuum to minimise the contamination of the freshly cleaved surface.

## 4.2. Debye-Waller measurement

Often when simulating materials, the sample temperature is set to 0 K. This creates a problem when comparing numerical with experimental data, as inelastic effects become more prominent at higher temperatures. To correct the results of the elastic CC-simulation, the temperature dependence of the scattering signal was determined by an experimental measurement.

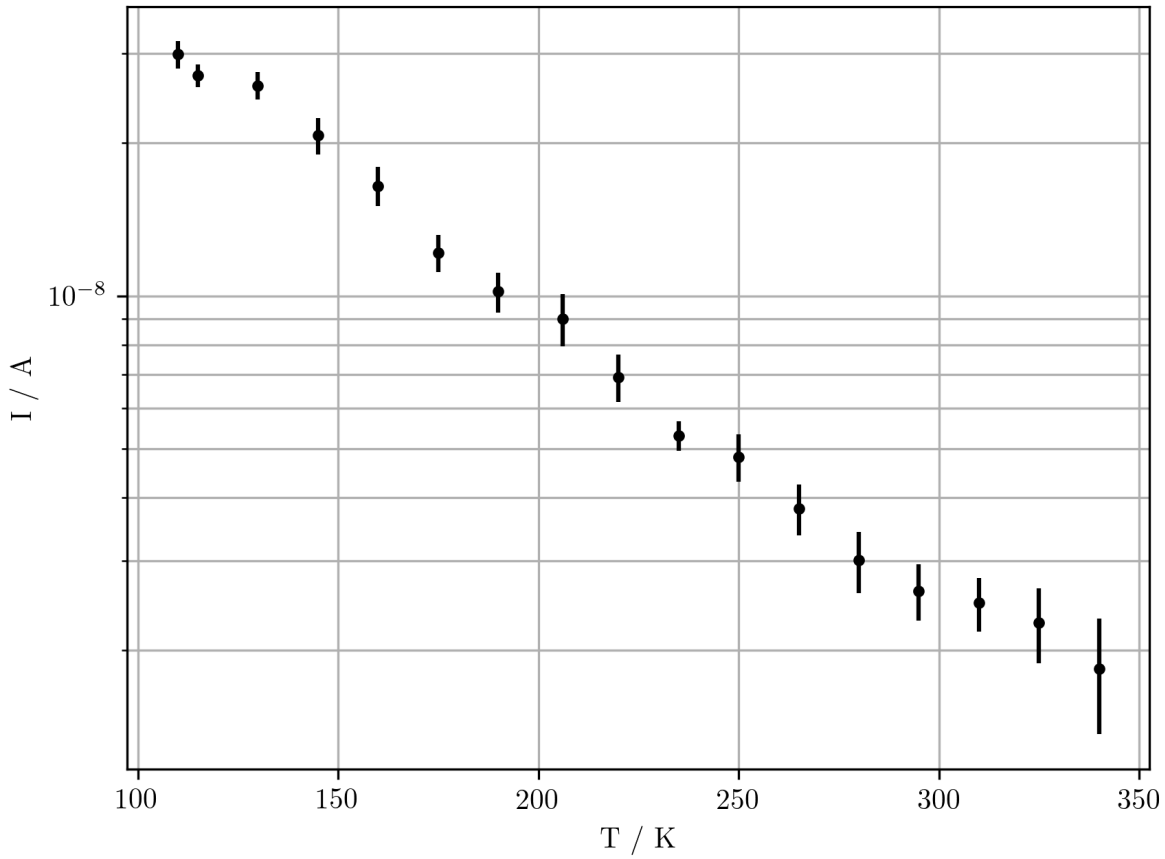


Figure 4.1.: Debye-Waller measurement: The surface temperature T can be seen on the x-axis using a linear scale and the detector current I at the specular position of $\theta = 22.2°$ is shown on the y-axis in logarithmic scale. This makes the linear/exponential behaviour visible, which can be used to determine the Debye-Waller factor.

The measurement, which assesses this dependency, is called Debye-Waller measurement, as it enables the determination of the Debey-Waller factor, which describes the attenuation of

the scattered helium signal for different amounts of thermal motion in the sample. In other words, it can be used to predict the signal intensity for different sample temperatures.

To obtain the needed data the scattered intensity is measured at a fixed position for different sample temperatures. For a good signal to noise ratio, it is advised to use the specular peak position as it produces the highest count rate, which is found at an azimuthal angle $\theta$ of 22.2° for the apparatus described in section 2.3. The actual measurement was then conducted with a beam energy of 8 meV with a small energy bandwidth of 0.6 meV(FWHM) along the $\overline{\Gamma\mathrm{M}}$ direction. To get a directly scattered beam both solenoid currents were set to 0 A and data points were taken at seventeen different sample temperatures ranging from 115 K to 340 K at a step size of 15 K and one at 110 K.

The measured points are listed in the appendix in table A.1 and are visualised in figure 4.1.

## 4.3. $\theta$-measurement

A measurement which can be used to identify SARs, calculate the surface corrugation and determine the surface lattice constant is the so called $\theta$-scan. This scan is done by changing the incident angle $\theta_i$ and measuring the scattered beam intensity like in the Debye-Waller measurement. For this, the solenoid currents are set to 0 A and the azimuthal angle $\phi$, the beam energy $E_{beam}$ and the temperature of the sample $T_s$ are set to fixed values.

To obtain more data points for the analysis, the scans were repeated with different values for the beam energy and the azimuthal angle using the same sample temperature of 112 K, as listed in Table 4.1.

In figure 4.2, the elastic peaks and an inelastic background can be seen. In between the peaks, there are also small changes in intensity which can be assigned to SARs. Those positions can be described by equation 2.13. By changing the beam energy and the azimuthal angle, different SAR conditions can be met.

Table 4.1.: List of $\theta$-scans of $Bi_2Te_3$ taken at a sample temperature of 112 K with different beam energies and azimuthal angles.

$N_\theta$ ... Number to identify the $\theta$-scan

$E_{beam}$ ... Helium beam energy in meV

$T_N$ ... Temperature of the helium nozzle in K

Orientation ... Azimuthal orientation of the sample

| $N_\theta$ | $E_{beam}$ | $T_N$ | Orientation |
|---|---|---|---|
| 0 | 11.63 | 54 | $\overline{\Gamma K}$ |
| 1 | 7.97 | 37 | $\overline{\Gamma K}$ |
| 2 | 7.97 | 37 | $\overline{\Gamma M}$ |
| 3 | 11.42 | 53 | $\overline{\Gamma M}$ |

The graphical representations of the other measurements listed in table 4.1 can be found in the appendix (figures A.1-A.3).

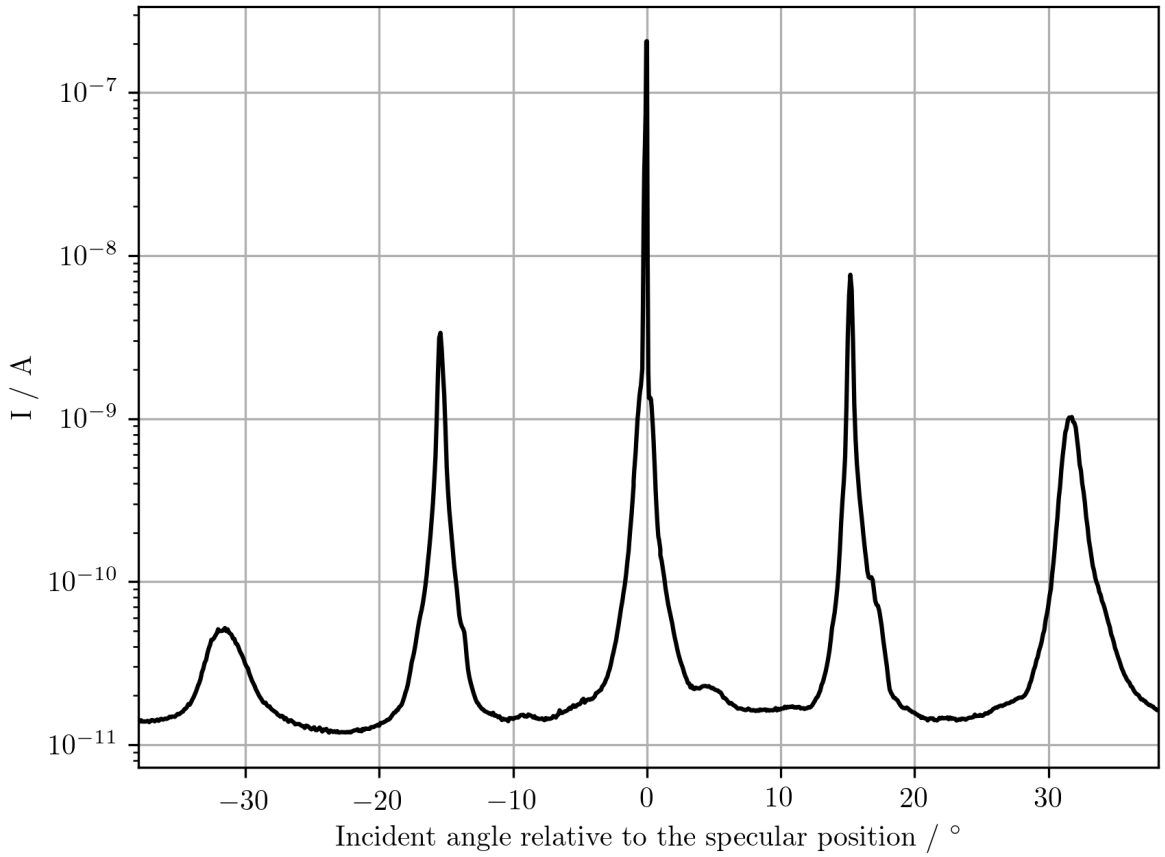


Figure 4.2.: $\theta$-scan 2: The detector current I versus the angle of incidence $\theta$ for $N_\theta$=2 using the scattering conditions found in Table 4.1. The elastic peaks, as well as an inelastic background with SAR features are observable.

## 4.4. Azimuthal-energy-measurement

The identification of a SAR can be quite difficult, as a shift in energy with respect to equation 2.13 can occur, due to inter channel coupling. Using the two-dimensional scan, which measures the scattered intensity depending on the azimuthal angle and the beam energy, the SARs show up as lines instead of single peaks. This eases identification, as certain scattering vectors can be identified by the curvature of the lines.

One option to acquire the two-dimensional data are many scans over the beam energy at different azimuthal angles, but the apparatus described in chapter 2.3 enables a fast

measurement of different beam energies using a method called Fourier-Transformed Spin Precession Spectroscopy [17]. In this method, the first solenoid is set to a certain value and the second solenoid current is set to 0 A.The beam is produced with a large spread in energy. Two measurements with one beam centered at 8 meV with a full width at half maximum of $(1.66 \pm 0.02)$ meV, and a second one around 11 meV with a width of $(3.80 \pm 0.03)$ meV were performed. Using these beams and measuring the scattered beam with respect to the different magnetic field strengths in the first solenoid, the scattered intensity distribution can be recovered by a Fourier transformation. Using this method, scans for different azimuthal angles were taken to produce a two-dimensional dataset.

Like in the Debye-Waller measurement, a good signal to noise ratio was achieved by measuring at the specular position of $\theta$=22.2° and a sample temperature of 110 K. The graphical representation of the dataset can be seen in figure 4.3, which shows a contour of the scattered intensity for different combinations of the beam energy and the azimuthal angle.

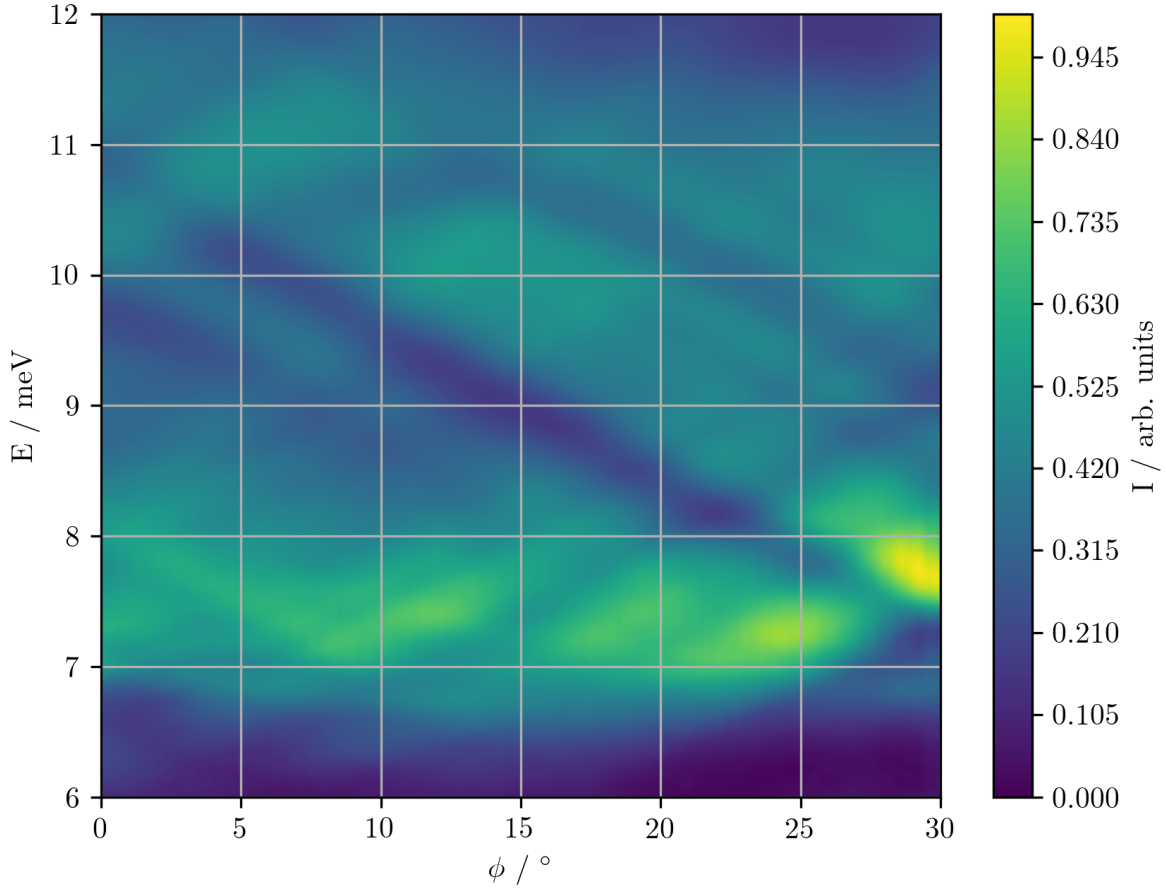


Figure 4.3.: Experimental azimuthal-energy-measurement: The specular intensity I for different beam energies E (y-axis) and azimuthal angles $\phi$ (y-axis) shown as a contour plot. Resonance features show up as lines in the intensity distribution, which are used to determine the bound state energies of the surface-interaction potential.

# 5. Analysis

In this chapter, the experimental data shown in chapter 4 is analysed. This includes the calculation of the lattice constant, the Debye-Waller Factor and the surface potential for $^3$He-$Bi_2Te_3$. To reduce the possibility of systematic errors for the potential parameters, two different methods are discussed.

## 5.1. Determination of the lattice constant

The lattice constant is important for many calculations. In the literature, values can be found for the bulk lattice constant. However, in the case of HAS the interesting lattice constant is the one observable on the sample surface, as helium does not penetrate into the bulk.

Using the elastic peak positions from table B.1, wave vectors $\mathbf{K}$ can be calculated for every observed peak by:

$$|\mathbf{K}| = |\mathbf{k_i}| \left[\sin(\theta_f) - \sin(\theta_i)\right] \tag{5.1}$$

The incident angle $\theta_i$ equals the peak position and the final scattering angle $\theta_f$ is the source-detector-angle minus the incident angle. The scattering vector $\mathbf{G}$ can be calculated by dividing the surface wave vector $\mathbf{K}$ by the order of the peak $n$.

$$|\mathbf{G}| = \frac{|\mathbf{K}|}{n} \tag{5.2}$$

Assuming no surface reconstruction, the sample surface is hexagonal and since the scattering direction of the measurement is known, $\mathbf{G}$ can be used to calculate estimates of the lattice constant $a$. For measurements in the $\overline{\Gamma\mathrm{M}}$-direction

$$a = \frac{4\pi}{\sqrt{3}\,|\mathbf{G}|} \tag{5.3}$$

was evaluated and for measurement in $\overline{\Gamma\mathrm{K}}$-direction, the following equation was used.

$$a = \frac{4\pi}{|\mathbf{G}|} \tag{5.4}$$

For every measurement from table 4.1 the average lattice constant from all peaks, were obtained as well as the standard errors. For the final value used in the simulation, the average of those lattice constants, weighted by the inverse of the variance, was calculated. The resulting values are listed in table 5.1.

Table 5.1.: Results of the surface lattice constant analysis, where $N_\theta = 0 - 4$ represents a weighted average of the other values

$\mathrm{N}_\theta$ ... Number of the used $\theta$-scans from table 4.1

a ... Average surface lattice constant in Å

$\Delta$a ... Standard error of the average surface lattice constant in Å

| $\mathrm{N}_\theta$ | a | $\Delta$a |
|---|---|---|
| 0 | 4.44 | 0.03 |
| 1 | 4.388 | 0.008 |
| 2 | 4.39 | 0.01 |
| 3 | 4.42 | 0.04 |
| Average | 4.39 | 0.01 |

Comparing the results in table 5.1 to the scattering parameters from table 4.1 one can notice that higher beam energies result in bigger lattice constants, but also a higher standard error.

Combining the results from all four measurements a surface lattice constant of $(4.39 \pm 0.01)$ Å was achieved. This value, as well as the measurements with lower beam energies, seem to be in good agreement with the literature, where a bulk lattice constant with a value of $(4.374 \pm 0.001)$ Å was found for a sample temperature of 110 K using X-ray diffraction [16].

## 5.2. Determination of the surface potential

When scattering helium off a surface, the helium atom has to pass a potential, which is zero far away from the surface, has a negative region where bound states can be located, and exhibits a repulsive part close to surface atoms. This potential, which is involved in the scattering process, cannot be measured directly as only measurements in the asymptotic region, where the potential is zero, are taken. This leaves only indirect methods, which use measurable effects caused by the interaction.

The process used in this thesis assumes a potential form and tries to validate it by comparing simulations using this potential with experimental data. This leads to a process, which is structured into the following steps:

1. Guess a two-dimensional potential
2. Determine the corrugation to acquire a three-dimensional potential
3. Simulate experimental results
4. Compare the simulation to experimental results

In the first step, a potential has to be guessed. This is done by evaluating at SAR positions, which correspond to bound states of the interaction potential and can be used to fit the potential parameters of the averaged potential.

One problem using this method is the fact that the resonances are not easy to identify and exhibit offsets when compared to the kinematic condition in equation 2.13. Looking at simulations, those offsets can be estimated, but a more accurate way involves sampling potential parameters close to the guessed position acquired from the SAR positions. Comparing the results from all those simulations with the measured results, the best parameter combination can be determined.

In the second step, a corrugation value is determined by simulating experimental properties and comparing them to experimental data. One property which can be used are the elastic peak areas, as their relative values depend on the surface corrugation. As seen in figure 5.3 this may lead to multiple results, which have to be considered.

Using the corrugation and the two-dimensional potential, CC-simulations are conducted, which are then compared to experimental data to assess the quality of the proposed potential.

## 5.3. Determination of the experimental peak areas

The peak intensity in $\theta$-scans is one attribute, which can be used to compare the elastic CC-simulation to the experimental results. It is important to note, that the elastic CC-simulation cannot simulate the correct peak intensity distribution, as it depends on inelastic effects, but it is capable of calculating the intensities of scattering channels, which are comparable to the peak area of elastic peaks, seen in the experimental data.

To get an accurate value for the peak areas, a scaled pseudo-Voigt profile was fitted to the peaks using the `curve_fit` function found in the `scipy.optimize` package. The pseudo-Voigt profile $V_p$, described in equation 5.5, is a combination of a Gaussian and a Lorentzian profile. $\theta_0$ is the peak position, $\eta$ describes the mixing of the Gaussian and the Lorentzian profile, $s$ is the scaling factor, and $2w$ is the full width at half maximum.

$$V_p(\theta) = s \left( \eta \cdot \underbrace{\frac{1}{\left(1 + \frac{\theta-\theta_0}{w}\right)^2}}_{Lorentz} + (1-\eta) \cdot \underbrace{e^{-\ln(2)\cdot\left(\frac{\theta-\theta_0}{w}\right)^2}}_{Gauss} \right) \quad \text{with} \quad 0 < \eta < 1 \tag{5.5}$$

The peak area $A$, is calculated by evaluating the linear combination of Gaussian and Lorentzian area:

$$A = \frac{s}{A_0} \left( \sqrt{\frac{\pi}{\ln(2)}} w(1-\eta) + \eta\pi w \right) \tag{5.6}$$

The areas were normalised for each spectrum setting the specular peak area $A_0$ to 1. Propagating the uncertainty of the fitted profile, the uncertainty of the areas is given

as

$$\Delta A = \frac{1}{A_0}\left[\left(\Delta s\left|\sqrt{\frac{\pi}{\ln(2)}}w(1-\eta)+\eta w\pi\right|\right)^2 + \left(\Delta w\left|s_n\sqrt{\frac{\pi}{\ln(2)}}(1-\eta)+\eta\pi\right|\right)^2 + \left(\Delta\eta\left|-s_n\sqrt{\frac{\pi}{\ln(2)}}w+w\pi\right|\right)^2\right]^{\frac{1}{2}} \tag{5.7}$$

and can be found in Table B.1 along with the fitted peak parameters and calculated areas.

## 5.4. Debye-Waller coefficient

The Debye-Waller coefficient W describes the attenuation of the helium beam due to increased inelastic scattering at higher sample temperatures. It is defined in equation 5.8 and can be determined by measuring the intensity $I$ of the scattered beam, while changing the sample temperature $T_S$.

$$I(T_s) = I(0)\cdot e^{-2WT_s} \tag{5.8}$$

The coefficient can be obtained by fitting a linear function to the logarithm of the intensity. From the resulting slope of $-2W$, $W$ can be determined. For $Bi_2Te_3$ a slope of $(-0.0131 \pm 0.0003)\,\mathrm{K}^{-1}$ and a Debye-Waller coefficient of $(0.0066 \pm 0.0002)\,\mathrm{K}^{-1}$ was found.

Because the attenuation of the signal can be linked to inelastic scattering events, the Debye-Waller coefficient can be related to the Debye Temperature $T_D$:

$$W = \frac{3\hbar^2(k_{zi}+k_{zf})^2}{2k_bT_D^2M} \tag{5.9}$$

The momentum transfer is calculated by using $k_{zi}$, the incident wave vector perpendicular to the surface, and $k_{zf}$, the wave vector perpendicular to the surface after the scattering event. The Boltzmann constant is written as $k_b$ and M is an effective surface mass [19].

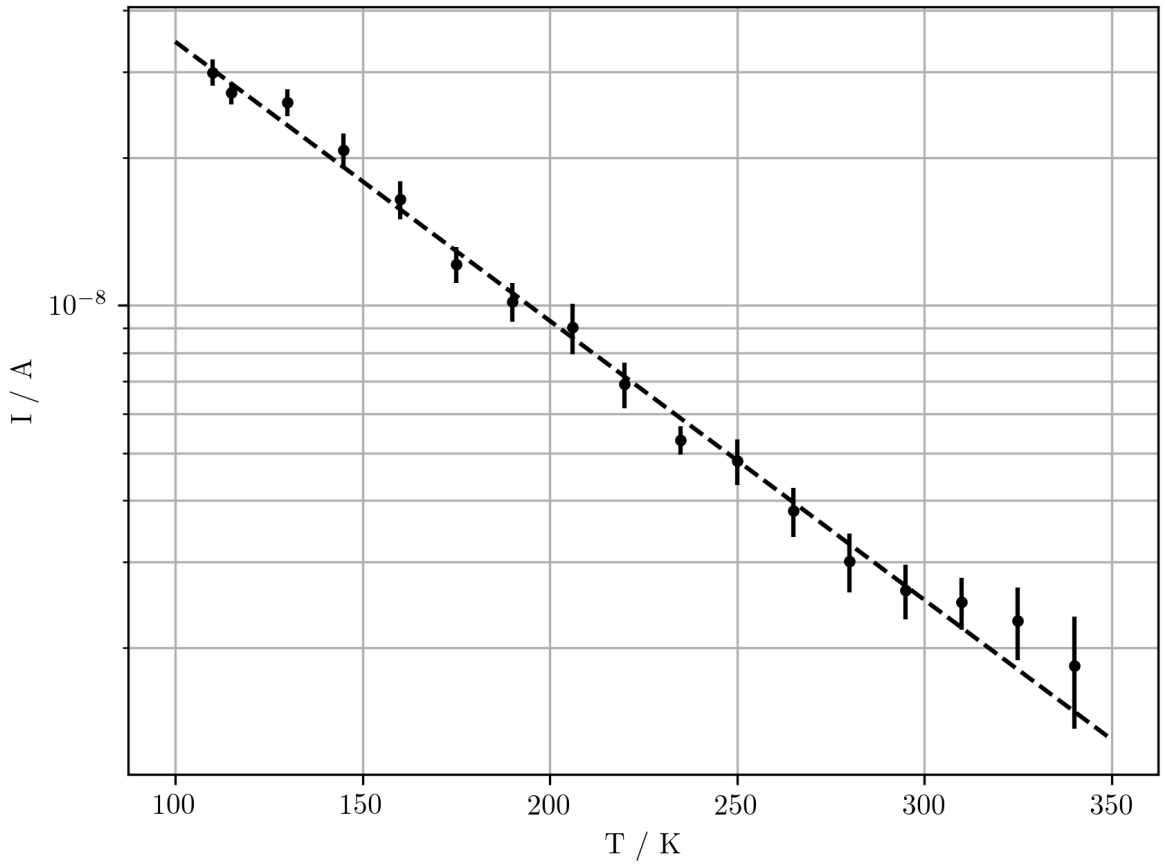


Figure 5.1.: Debye-Waller measurement with linear fit: Using a logarithmic scale for the intensities reveals the linear nature regarding the sample temperature. Using this, a Debye-Waller coefficient of $(0.0066 \pm 0.0002)\,\mathrm{K}^{-1}$ can be calculated [18].

Using the Beeby correction, $k_{zi}$ and $k_{zf}$ can be expressed as seen in equations 5.10 and 5.11. Here the potential depth $D$ and the beam energy $E_i$ are used to correct for the acceleration of the helium atom near the surface. To get the surface normal part of the wave vectors, $\theta_i$ and the sensor-detector angle $\theta_{SD}$ are used [19].

$$k_{zi} = k_i \sqrt{\cos^2(\theta_i) + \frac{D}{E_i}} \tag{5.10}$$

$$k_{zf} = k_i \sqrt{\cos^2(\theta_{SD} - \theta_i) + \frac{D}{E_i}} \tag{5.11}$$

The wave vector $k_i$ of an atom beam, is calculated using the definition of the de Broglie wavelength and the kinetic energy, which is shown in equation 5.12, where $m_{^3\mathrm{He}}$ is the

projectile mass of a single $^3$He atom [20].

$$E_i = \frac{k_i^2 \hbar^2}{2m_{^3\mathrm{He}}} \tag{5.12}$$

Using equations 5.9 to 5.12 and the experimental data from table A.1, the Debye Temperature can be calculated for a given potential depth and an effective mass. However the effective mass cannot be measured directly, so for further calculations $\alpha = T_D^2 \cdot M$ was used. Using a potential depth of 6.22 meV results in $\alpha = (1.39 \pm 0.03) \times 10^{-21}\,\mathrm{K^2\,kg}$.

## 5.5. Resonance identification

One way to obtain a good initial two-dimensional interaction potential, uses SARs, as they depend on the bound states of the potential. Using the kinematic condition in equation 2.13 the resonance positions can be calculated using a scattering vector $\mathbf{B}$ and a bound state energy $\epsilon_n$. This enables the matching of a calculated position to a peak or dip in the measurement, which leads to the corresponding scattering vector and bound state energy pair.

Equation 2.13 is, however, based on the free atom model, which assumes a sample with no surface corrugation. This causes the predicted bound state energies to be incorrect when applied to highly corrugated surfaces. The reason for this deviation is a band deformation introduced by the corrugated potential, which is similar to the one observed in the free electron model, where the bands bend at the edge and the center of the Brillouin zone and create gaps [9]. Nevertheless, can these bound states be used to approximate the initial surface potential. To correct the bound states predicted by the free atom model a shift is introduced, which is given as the energy difference between the energies found for the corrugated potential and the free atom model.

To determine these shifts an initial potential using the free atom model is created, by identifying SARs in $\theta$-scans or azimuthal-energy scans. The shifts, however, make the identification of the resonances in $\theta$-scans quite difficult [21, 22]. Therefore, the data of the two-dimensional scan was used. It has the advantage of not only seeing the SAR position on the energy scale, but also the dependence on the azimuthal angle, which can be used to determine the scattering vector. To calculate the positions, the kinematic

condition from equation 2.13 was written in terms of the incident angle $\theta_i$ and the incident wave vector $k_i$, which corresponds to the beam energy as well as the components of the scattering vector $B_\parallel$ and $B_\perp$ parallel and perpendicular to the scattering direction:

$$-\cos^2(\theta_i)k_i^2 + 2\sin(\theta_i)B_\parallel k_i - |\epsilon_n| + B_\perp^2 + B_\parallel^2 = 0 \tag{5.13}$$

Using this equation, an overlay for the experimental data, seen in figure 5.2 can be drawn, which is used to identify some resonances by plotting lines for many scattering vectors and looking at the resonance shape. The resonance position on the energy axis could then be adjusted by selecting an appropriate bound state energy. This leads to the initial two-dimensional potential. Investigations of the dependency between the resonance positions and the potential parameters using CC-simulations enabled additional SAR identifications. All found SARs that are used in further investigations can be seen in figure 5.2 and are listed in table 5.2.

By comparing the simulated data from the CC-simulations seen in figure 5.6 to the prediction of the kinematic condition the offsets $\epsilon_{\text{off}}$ for the bound states energies can be determined. These offsets range from $-0.68\,\text{meV}$ to $0.46\,\text{meV}$, which are similar to the offset found for the ground state of the $^4$He-NaCl(001) potential, where a correction greater than $0.5\,\text{meV}$ was applied [9]. It illustrates that band structure effects play a significant role for the He-$Bi_2Te_3$(111) interaction potential. Hence CC-simulations are necessary for an exact determination of the interaction potential.

Table 5.2.: List of experimental resonances: This table contains the resonances, which could be identified in the experimental data. A resonance is defined by the scattering vector and a bound state. The offsets determined after simulating the measurement and comparing the SAR positions with the free atom model are also listed.

No. ... Number of the found resonance

$d_1$ ... The first index of the scattering vector

$d_2$ ... The second index of the scattering vector

$\epsilon$ ... Bound state energy of the resonance in meV

$\epsilon_{\text{off}}$ ... Offset between the kinematic condition and the resonance emerging from the simulation shown in figure 5.6 in meV

| No. | $d_1$ | $d_2$ | $\epsilon$ | $\epsilon_{\text{off}}$ |
|---|---|---|---|---|
| 0 | 2 | −1 | 2.1 | −0.68 |
| 1 | 1 | 2 | 0.4 | −0.12 |
| 2 | 1 | −2 | 0.1 | 0.42 |
| 3 | 0 | 2 | 0.4 | −0.08 |
| 4 | 2 | −2 | 1.7 | 0.08 |
| 5 | 1 | 1 | 0.1 | 0.46 |
| 6 | 0 | 2 | 4.1 | 0.43 |
| 7 | 1 | −2 | 1.9 | 0.09 |
| 8 | 1 | −3 | 4.9 | −0.44 |

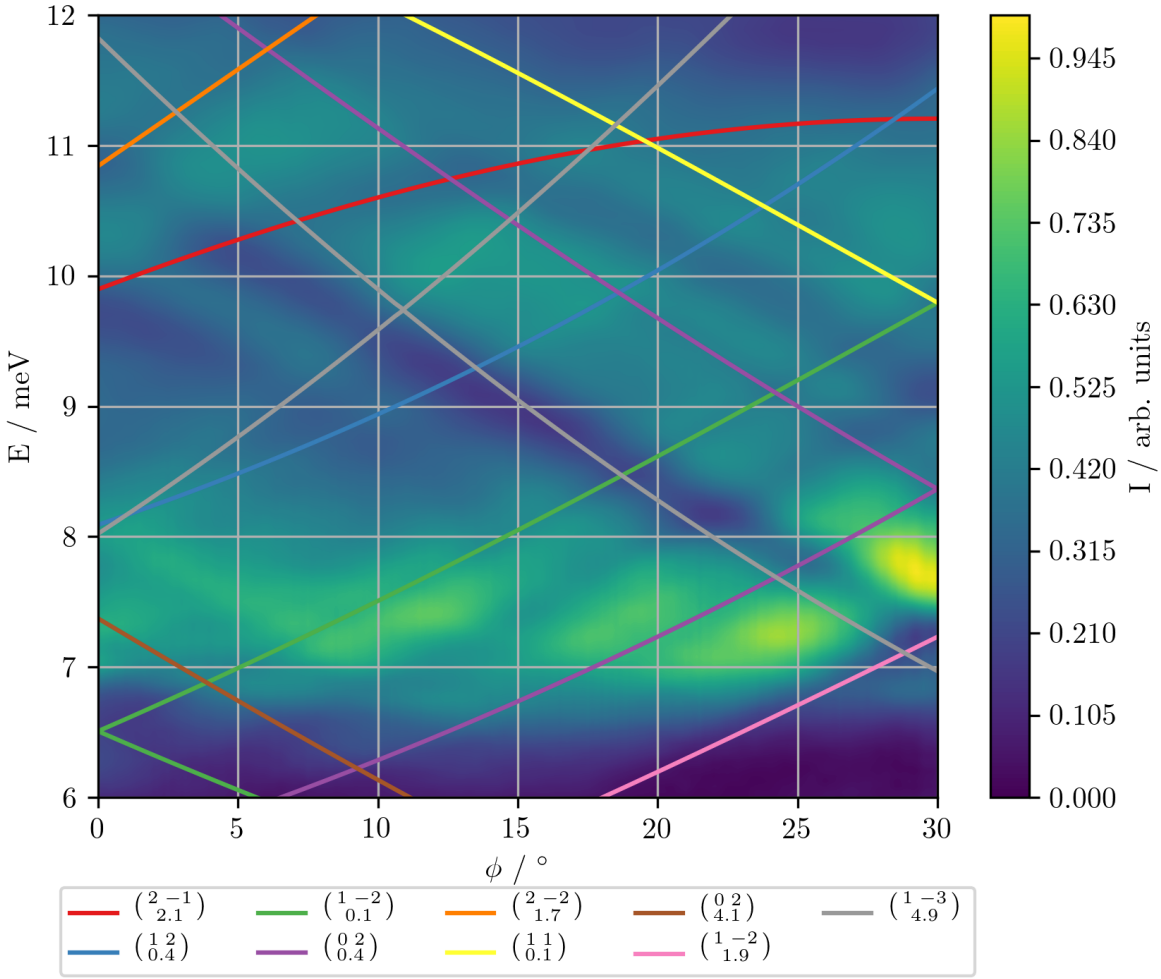


Figure 5.2.: Azimuthal-energy measurement with a kinetic SAR conditions overlay: The experimental data from the energy-azimuth scan is plotted as a contour plot with an overlay of matching kinematic SAR conditions. The resonances seen as dips and peaks can then be used to fit an interaction potential. Some features seen in the experimental data are not used as they could not be assigned to a unique resonance.

## 5.6. Determination of the potential by fitting bound states

If the bound state energies of the averaged potential can be calculated fast enough it is feasible to use the bound state energies from table 5.2 to fit the surface potential. Using the CMP, the bound states $\epsilon_n$ can be calculated analytically using equation 5.14. This enables the use of an optimisation routine to be written, which results in potential parameters of D=$(6.4 \pm 0.3)$ meV and $\kappa$=$(0.94 \pm 0.06)$ Å$^{-1}$, describing a potential with three bound states at 4.54 meV, 1.82 meV and 0.32 meV.

$$\omega = \kappa\sqrt{\frac{2D}{m_{^3\mathrm{He}}}}; \quad \gamma = \frac{2D}{\hbar\omega}; \quad \epsilon_n = -D + \hbar\omega(n+0.5)\left(1 - \frac{n+0.5}{2\gamma}\right) \tag{5.14}$$

To find the corrugation for the three-dimensional potential the elastic peak intensities are simulated with the elastic CC-simulation and compared to the peak areas from table B.3, which only gives a useful result if the simulated intensities are adjusted to the correct sample temperature using the Debye-Waller factor, determined in section 5.4.

The simulations for the corrugation search were done using a search range for the corrugation parameter $h$ of 0.0001 to 0.1 with a step width of 0.001 and an integration range for the z direction of $-4$ Å to 17 Å. The lattice constant was set to 4.39 Å. In order to get a converging signal, an absolute error of $10^{-7}$, 92 closed channels, all open channels and a step width for z, ninety times smaller than the smallest observed scattering channel wavelength, were used.

For every $h$ value, the simulated data was used to evaluate the cost function $C$.

$$C = \sum_i^l \sqrt{\frac{(A_{i,s} - A_{i,m})^2}{l}} \tag{5.15}$$

This function subtracts the peak areas $A_{i,m}$ from table B.3 from the simulated normalised peak height $A_{i,s}$ and sums over all peaks except the specular one, as they were always set to one in both cases. The number of peaks without the specular ones is given by $l$.

The resulting data is shown in figure 5.3, where a local minimum can be seen at $h$=0.068 and a global minimum at $h$=0.021. As both minima could be correct, further simulations were made to decide on the correct one.

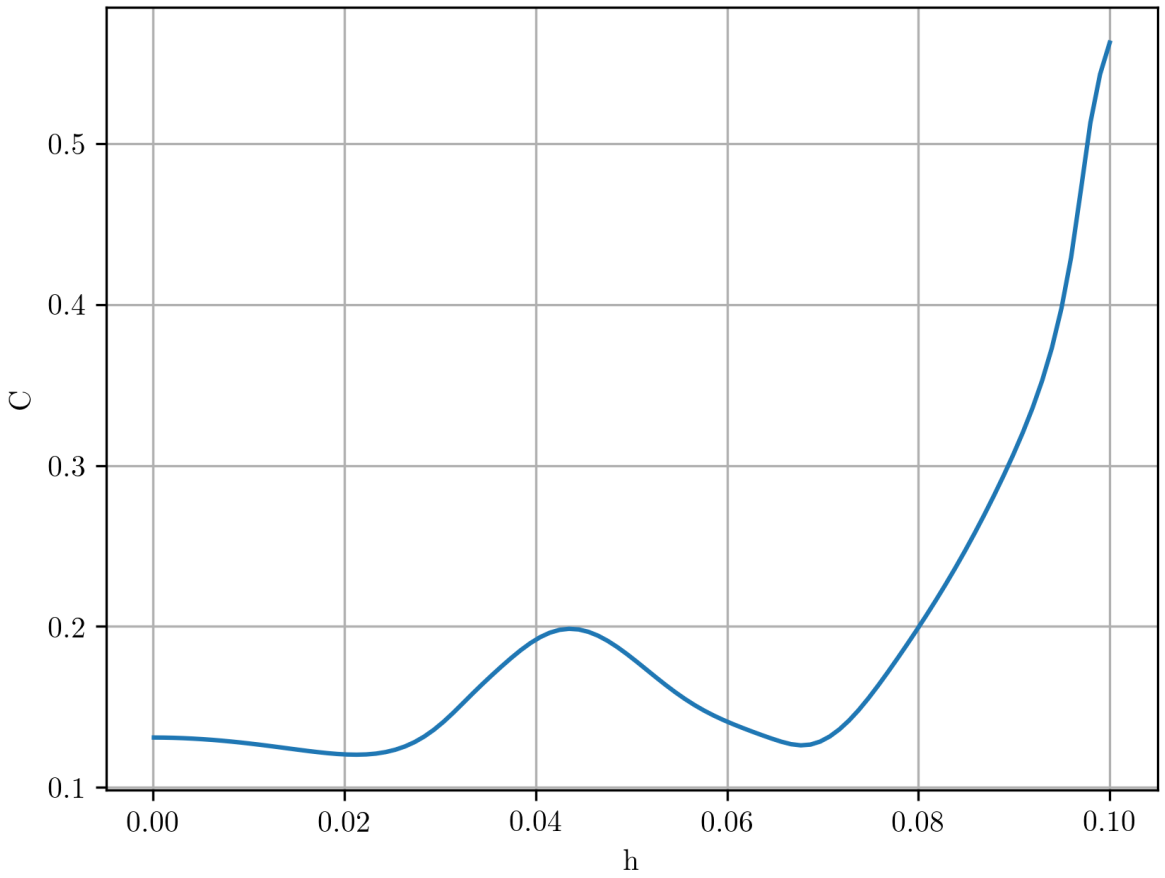


Figure 5.3.: Corrugation cost function: The cost function $C$ is shown for different values of $h$ for a potential with the parameters $D = 6.355\,\text{meV}$ and $\kappa = 0.938\,\text{Å}^{-1}$. with a minimum at $h = 0.0677$ and another one at 0.021

A good way to decide on the correct corrugation value is a comparison to the experimental resonance positions. This leads to two azimuthal scans being simulated and plotted with an overlay of the kinematic resonance conditions for the bound state energies found in table 5.2.

Comparing the two simulations from figure 5.4 and 5.5 the higher corrugation shows a better reproduction of the background signal, as well as the resonance positions. Especially the resonances $\binom{1}{0}^{-3}$ and $\binom{1}{0}^{2}$ are missing in the low corrugation simulation. This makes the simulation seen in figure 5.4 more likely to be correct and therefore this simulation is further investigated.

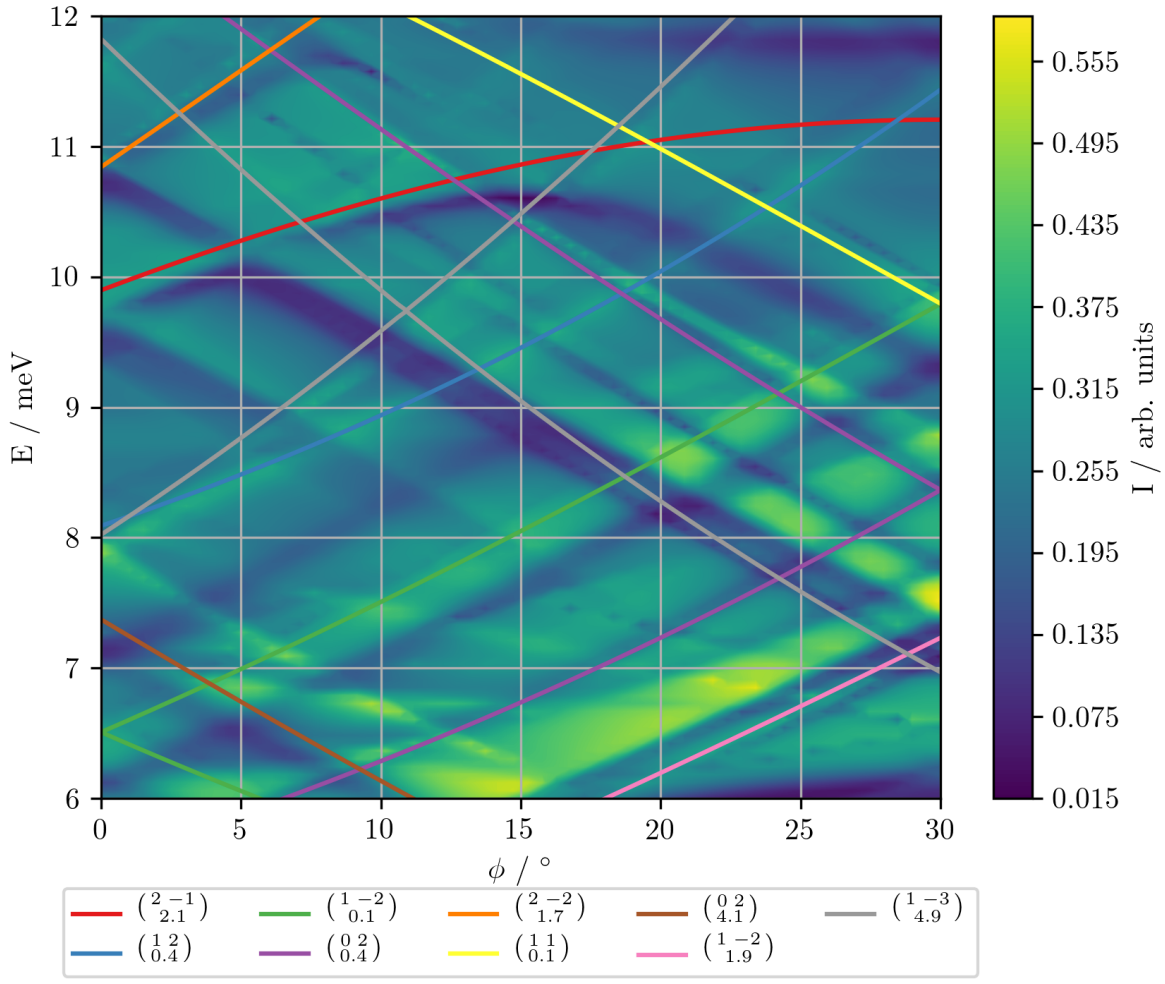


Figure 5.4.: Azimuthal CC-simulation for the higher corrugation value: A simulation of an azimuthal scan using a potential with D = 6.355 meV, $\kappa = 0.938\,\text{Å}^{-1}$ and h = 0.0677. The SAR positions extracted from the experimental data are shown as lines and a correspondence for every resonance can be seen in the simulated data.

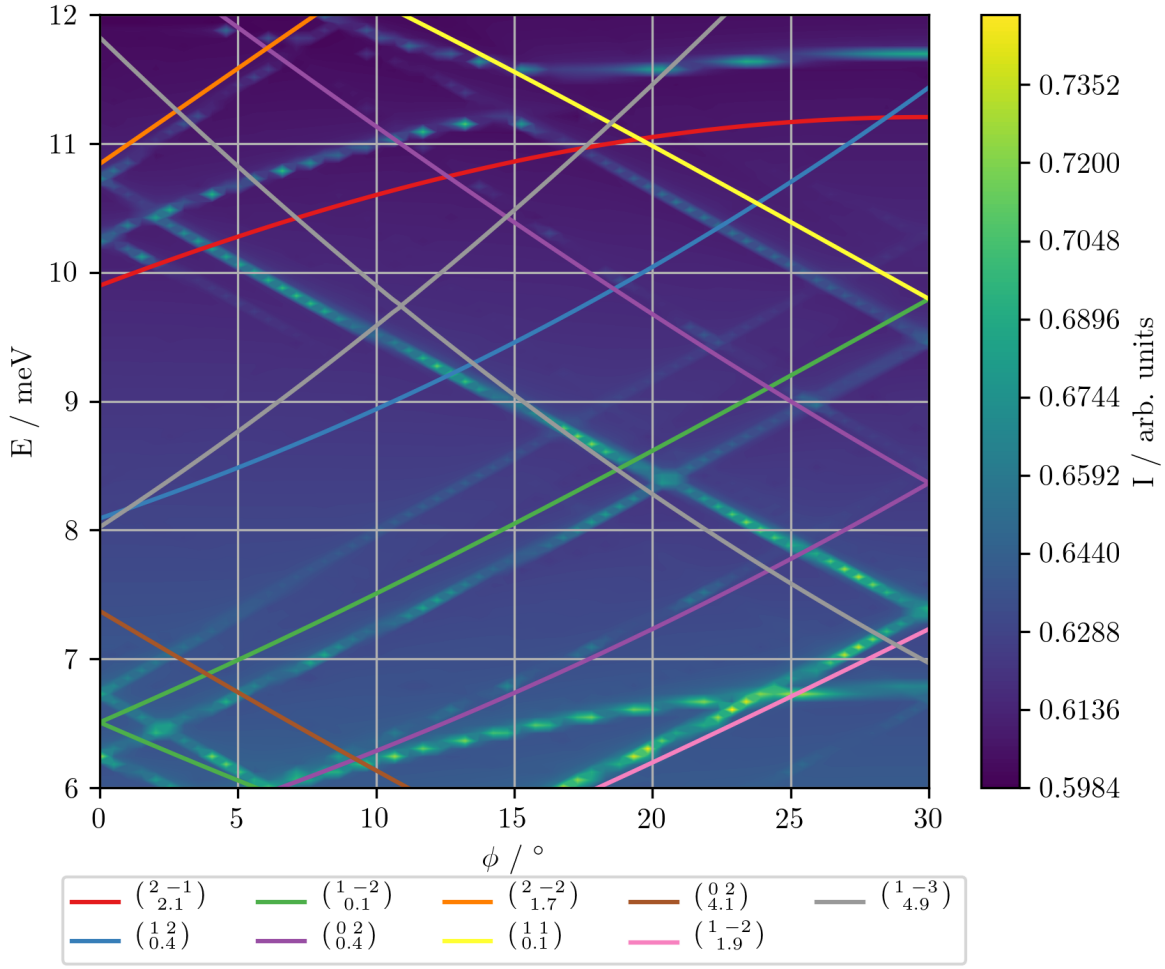


Figure 5.5.: Azimuthal CC-simulation for the lower corrugation value: The elastic CC-simulation using the potential parameters D = 6.355 meV, $\kappa = 0.938\,\text{Å}^{-1}$ and h = 0.021 with the resonance positions found in the experimental data is shown. This simulation shows less background intensity and also misses some resonances, which were clearly observed in the experimental data

When plotting the resonances for the experimental bound state energies using the closest energy levels from the fitted potential, there is a shift in energy between the kinematic condition shown by the lines and the resonances in the simulated data. This indicates that the energies obtained in table 5.2 exhibit an offset $\epsilon_{\text{off}}$. The values found in this table are taken from the simulation seen in figures 5.6 and 5.4, and can be explained by the coupling between the scattering channels used in the CC-simulation [10].

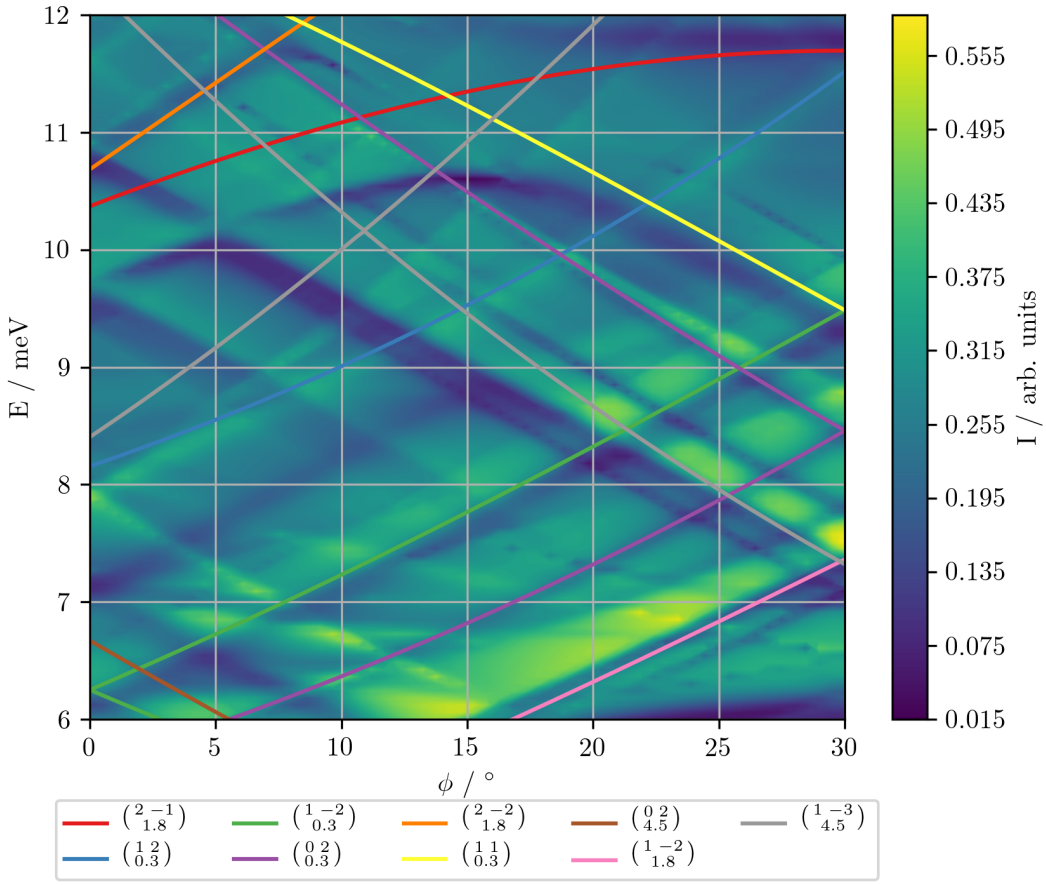


Figure 5.6.: Resonance shift: Comparing the resonance positions visible in the simulated data, seen in figure 5.4, to the kinematic conditions obtained by the bound states of the potential used in the simulation, an offset is observed. This offset seems to be different for every SAR and is listed in Table 5.2. A possible reason for this is the interaction of the scattering channels, which is not taken into account for in the kinematic model used for the overlaid lines.

Using these shifts in energy, an attempt to improve the fitted two-dimensional potential was taken. For this, the bound state energies and offsets from table 5.2 were added

together and a new set of parameters for the Morse-potential was fitted. This resulted in a new potential with the parameters D=$(6.2 \pm 0.2)$ meV and $\kappa$=$(0.92 \pm 0.05)$ Å$^{-1}$. To get the corrugation, a search was performed with the new potential in the same way as for the previous potentials, which led to a minimum of the cost function at $h$=$(0.07 \pm 0.02)$ The simulated data with the experimental SAR lines can be seen in figure 5.7. As the bound states for the new potential are similar to the one without the shift correction, the improvement is small but can be seen at the resonances $\left(\begin{smallmatrix} 0 & 2 \\ 0 & \end{smallmatrix}\right)$ and $\left(\begin{smallmatrix} 1 & -3 \\ 0 & \end{smallmatrix}\right)$.

To estimate the potential depth $D$ the ratio between the potential depth and the average atomic mass of the sample can be used. This yields a value of 0.039 meV u$^{-1}$ for the $Bi_2Te_3$(111) surface, which is in good agreement with similar materials like Sb and Bi, when compared to the respective ratios. For Sb(111) a ratio of 0.035 meV u$^{-1}$ [12] was found and Bi(111) was shown to have a ratio of 0.038 meV u$^{-1}$ [23].

The peak to peak corrugation of $Bi_2Te_3$ is 10 % of the surface lattice constant, which is about twice the corrugation found for the Bi(111) surface (4.63 % [23]), but smaller than the 13.6 % [12] of the Sb(111) surface.

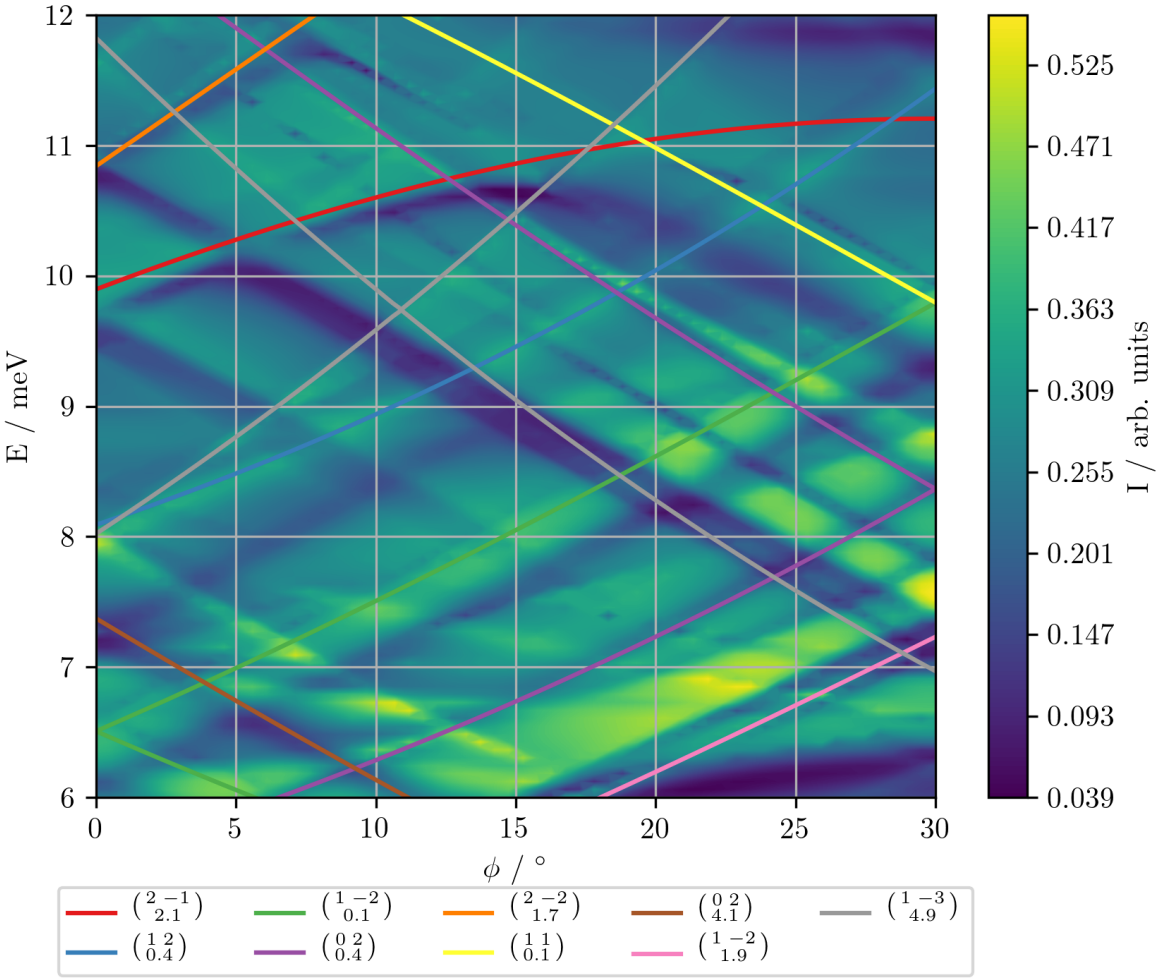


Figure 5.7.: Azimuth-energy CC-simulation after shift correction: Using the shift from the simulation seen in figure 5.6 the new fitted potential results in this slightly improved simulation result. The potential parameters used are D = 6.20 meV, $\kappa = 0.915\,\text{Å}^{-1}$ and $h = 0.070$. To enable a direct comparison of the resonance positions an overlay showing the kinematic conditions determined by the experimental data was added.

## 5.7. Determination of the potential by testing for resonance positions

In chapter 5.6, the potentials were determined by fitting bound states found from SARs in the experimental data. Due to the shift in the SAR positions, which depends on the potential, the best potential parameters are hard to find. Therefore, a self-consistency cycle or a method which does not use the bound state energies has to be evaluated to avoid this problem. The latter can be achieved by comparing the SAR positions directly to the experimental data, which requires the simulation of experimental results for a high number of parameter sets. To make this option viable, the search space has to be reduced, so that it can be scanned in a reasonable amount of time. This is done by using the potential found by the fitting method as the centre of the parameter space and creating a parameter grid around it, which reduces the number of simulations and enables the application of parallel computation.

In the case of the Morse potential, this parameter space is two-dimensional as $h$ can be determined by the minimum of the cost function seen in equation 5.15. To quantify the goodness of the resulting simulation, a $\chi^2$-test is used, testing that the SAR positions are at the experimental positions. This leads to an equation for the $\chi^2$ sum, which adds the squares of the difference between the position of the resonances from the simulations $\epsilon_{i,s}$ and the position seen in the experimental data $\epsilon_{i,m}$ divided by the sum of the standard deviations of the experiment $\sigma_{i,m}$ and the simulated data $\sigma_{i,s}$.

$$\chi^2 = \sum_i \left( \frac{\epsilon_{i,s} - \epsilon_{i,m}}{\sigma_{i,m} + \sigma_{i,s}} \right)^2 \tag{5.16}$$

Here the assumption that the resonance positions follow a normal distribution is taken, because they were measured by hand using the image analysis tool called Fiji on graphical representations of the simulation as seen in figure 5.7. To obtain the standard deviation, a cut at a fixed azimuthal angle was taken and the half width at half maximum of the resonance signal was used, after subtracting the background.

The calculation of the $\chi^2$ value is done on a grid with the potential depth $D$ spanning from 5.9 meV to 6.4 meV with a step width of 0.1 meV and the potential stiffness $\kappa$ spanning from 0.88 $\text{Å}^{-1}$ to 1.00 $\text{Å}^{-1}$ with a step width of 0.005 $\text{Å}^{-1}$ resulting in 143 potentials. The

resonances used in the calculation of the cost function are $\binom{0}{0.4}^{2}$, $\binom{2}{2.1}^{-1}$ and $\binom{1}{4.9}^{-3}$, which leads to three degrees of freedom. To visualise the result, the difference between the resonance positions in the simulation and the experiment are interpolated by a bivariate Spline before evaluating the cost function. This leads to figure 5.8, which also shows contours for different significance levels $\alpha$ of 1 %, 2 % and 5 %. Using these significance levels three parameter sets were determined, which are listed in table 5.3.

Table 5.3.: Potential parameters for different statistical significance levels

$\alpha$ ... the significance level

$D$ ... the potential depth

$\Delta D$ ... $\pm$ range of the potential depth

$\kappa$ ... the stiffness potential

$\Delta\kappa$ ... $\pm$ range of the potential stiffness

h ... the potential corrugation parameter

$\Delta$h ... $\pm$ range of the potential corrugation parameter

| $\alpha$ | $D$ | $\Delta D$ | $\kappa$ | $\Delta\kappa$ | h | $\Delta$h |
|---|---|---|---|---|---|---|
| 1 | 6.22 | 0.01 | 0.933 | 0.003 | 0.0637 | 0.0003 |
| 2 | 6.22 | 0.05 | 0.93 | 0.01 | 0.064 | 0.001 |
| 5 | 6.2 | 0.1 | 0.93 | 0.03 | 0.066 | 0.004 |

Compared to the results from Chapter 5.6 the uncertainty improved, while increasing the stiffness $\kappa$ and reducing the corrugation. The improved uncertainty enables the use of the potential in inelastic simulations, where instead of the Debye-Waller factor the temperature dependence is simulated by the Debye Temperature, the surface particle mass and a Gaussian cutoff factor. Because these parameters increase the search space even further, good potential parameters are essential to keep the search for the inelastic simulation parameters viable.

The peak to peak corrugation relative to the lattice constant is now a bit lower with a

value of $(9.6 \pm 0.2)\,\%$, which is higher than the corrugation found in metals and similar to the corrugation of semimetals like graphite(0001), which has a peak to peak corrugation of $8.6\,\%$ [24].

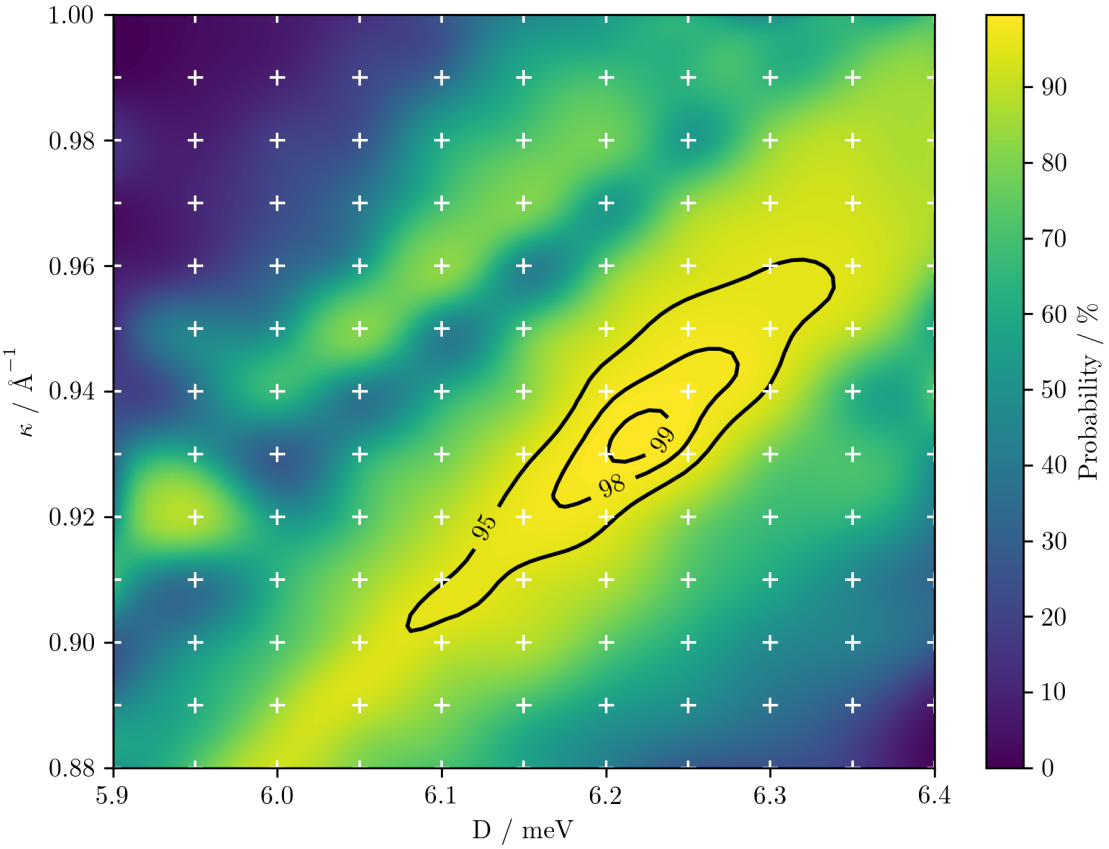


Figure 5.8.: The probability that the resonances $\binom{0}{0.4}\,\binom{2}{}$, $\binom{2}{2.1}\,\binom{-1}{}$ and $\binom{1}{4.9}\,\binom{-3}{}$ are the same in the experiment and the simulation. The white crosses show the evaluated points on the parameter grid and the contour lines show regions for $\alpha$-values of $1\,\%$,$2\,\%$ and $5\,\%$.

# 6. Summary

In the course of this work, a process is applied to find a good interaction potential for the $Bi_2Te_3(111)$ surface using helium atom scattering measurements and elastic close-coupling simulations. Helium atom scattering is used to obtain two basic material properties, which are needed for the simulations to compare the results with real measurements. The first one is the surface lattice constant, which usually is different from the bulk lattice constant, due to relaxation effects occurring on the surface. Using the elastic peak positions from the $\theta$-scans, this lattice constant is determined to be $(4.39 \pm 0.01)$ Å. In the literature, a value for the bulk lattice constant of $(4.374 \pm 0.001)$ Å at a sample temperature of 110 K is found, which is measured using X-diffraction and falls into the range of the value obtained by HAS [16]. This suggests that no surface reconstruction takes place and a hexagonal lattice structure can be assumed for the surface. The other property used to compensate for the lack of inelastic effects in the simulation is the Debye Waller coefficient. It is determined by analysing the temperature dependant specular peak height, which results in a factor $W = (0.0066 \pm 0.0002)\,\mathrm{K}^{-1}$. This can also be used to determine the surface Debye temperature if the effective surface mass and the potential depth is known. In case of the compound material $Bi_2Te_3(111)$ the effective surface mass is unknown, for which reason only the product of the Debye temperature squared and the effective mass, using a potential depth $D = 6.22\,\mathrm{meV}$, is calculated. Evaluating this product yields a value of $(1.39 \pm 0.03) \times 10^{-21}\,\mathrm{K^2\,kg}$, which is used for the inelastic close-coupling simulation.

Surface adsorption resonances are identified in the two-dimensional azimuth-energy scan. Those are then used to obtain the initial averaged surface potential by fitting the bound state energies of the resonances to the bound states of a Morse potential. A better potential could be obtained by the inclusion of resonances found between the elastic peaks of the $\theta$-scans, but their identification turned out to be difficult, as shifts introduced

by the interaction between the scattering channels are not included in the free atom model used in the identification process. Using the initial potential the corrugation for the three-dimensional potential is determined by optimising the simulation for the peak intensities of the $\theta$-scans. With this first three-dimensional potential the observed resonance shifts were determined and corrected in a second run, which resulted in a corrugated Morse potential with the following parameters:

$$D = (6.2 \pm 0.2)\,\text{meV} \qquad \kappa = (0.92 \pm 0.05)\,\text{Å}^{-1} \qquad h = 0.07 \pm 0.02$$

The offset between the resonance position to the kinematic resonance condition is in the range of $-0.68\,\text{meV}$ to $0.46\,\text{meV}$. Since those offsets also depend on the potential, a self-consistency cycle is needed for the process described above. This is avoided because automatic detection of the offset is not a trivial task. Instead, a different approach is taken using the potential found previously. In this approach, a global minimum is searched for by evaluating a cost function in parameter space applying a $\chi^2$-test testing the hypothesis that simulated resonance positions match the experimental ones. For this purpose, three resonances were chosen, as the initial potential showed three bound states. The result is a probability for the hypothesis to be true for points in parameter space around the initial potential. Selecting a significance level of $\alpha$=2 % leads to a good set of potential parameters with smaller tolerances as in the previous parameters. Those new parameters are:

$$D = (6.22 \pm 0.05)\,\text{meV} \qquad \kappa = (0.92 \pm 0.01)\,\text{Å}^{-1} \qquad h = 0.064 \pm 0.001$$

The peak to peak corrugation is calculated with the $h$ value, which yields $(0.420 \pm 0.007)$ Å or $(9.6 \pm 0.2)$ % of the lattice constant. Bi(111) has about half the corrugation of 4.63 % [23], whereas the Sb(111) surface exhibits a higher corrugation of 13.6 % [12]. One material with a similar corrugation is graphite, which shows a value of 8.6 % on its (0001) surface [24]. Thus, the value is similar to other semimetals, despite having an insulating bulk and metallic surface states. This could be explained by a combination of the Smoluchowski effect, which can smooth out the electron-density in metals and the localized electron-density found in insulating materials.

The potential depth $D$ is lower than the one found for Bi(111), which shows a value of $D$=$(7.9 \pm 0.1)\,\text{meV}$ [23] and higher than the potential depth found in Sb(111) (4.275 meV

[12]). This is expected, since the potential depth correlates with the atomic mass for similar materials, as heavier atoms are easier to polarize.

In this study, inelastic surface interactions are not yet considered. However, they are important, as they can lead to different resonance profiles, explain the temperature dependent scattering amplitudes and give insights into the electron-phonon interactions. Switching to inelastic close-coupling simulations, however, introduces new parameters and increases the computation time. Therefore, having a good elastic potential to start with is essential to achieve converging simulations.

# Appendix

# Appendix A.

# Data from measurements

Table A.1.: Debye-Waller measurement: Sample temperature $T$ and the detector current $I$ with its error $\Delta I$ from the Debye-Waller measurement of Bi2Te3 [18]

| T/K | I / nA | ΔI / nA |
|---|---|---|
| 110 | 29.9 | 1.8 |
| 115 | 27.2 | 1.4 |
| 130 | 26.0 | 1.6 |
| 145 | 20.7 | 1.7 |
| 160 | 16.5 | 1.5 |
| 175 | 12.1 | 1.0 |
| 190 | 10.2 | 0.9 |
| 206 | 9.0 | 1.1 |
| 220 | 6.9 | 0.7 |
| 235 | 5.3 | 0.4 |
| 250 | 4.8 | 0.5 |
| 265 | 3.8 | 0.4 |
| 280 | 3.0 | 0.4 |
| 295 | 2.6 | 0.3 |
| 310 | 2.5 | 0.3 |
| 325 | 2.3 | 0.4 |
| 340 | 1.8 | 0.5 |

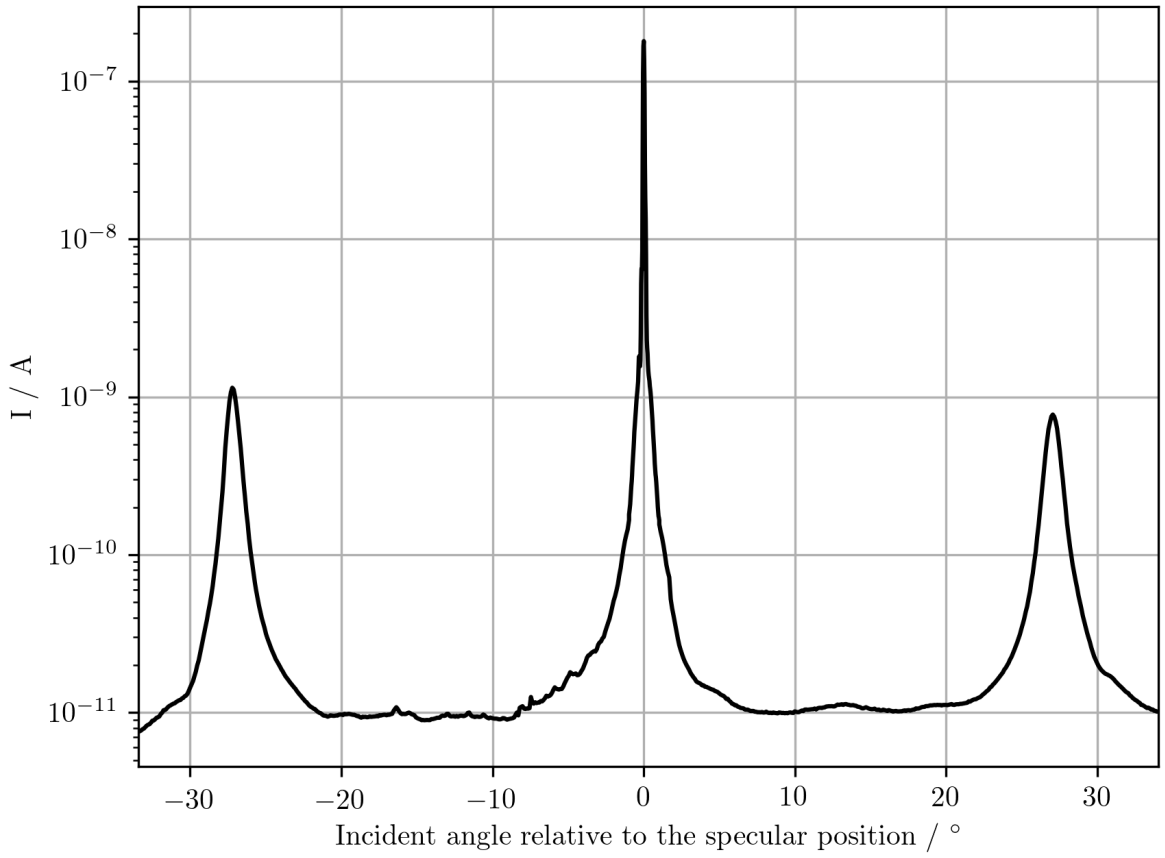


Figure A.1.: $\theta - scan1$: Scattered beam intensity versus angle of incidence $\theta$ of the measurement $N_\theta = 1$.

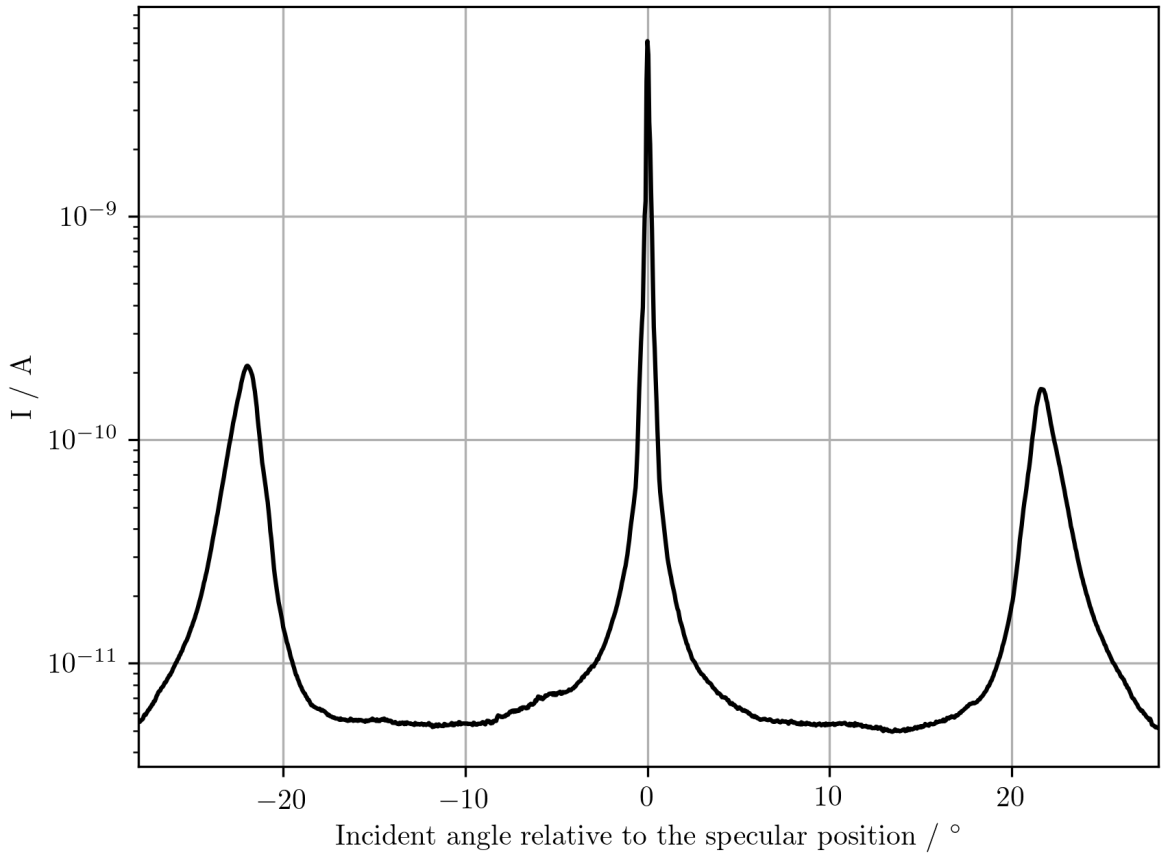


Figure A.2.: $\theta$-scan 0: Scattered beam intensity versus angle of incidence $\theta$ of the measurement $N_\theta = 0$.

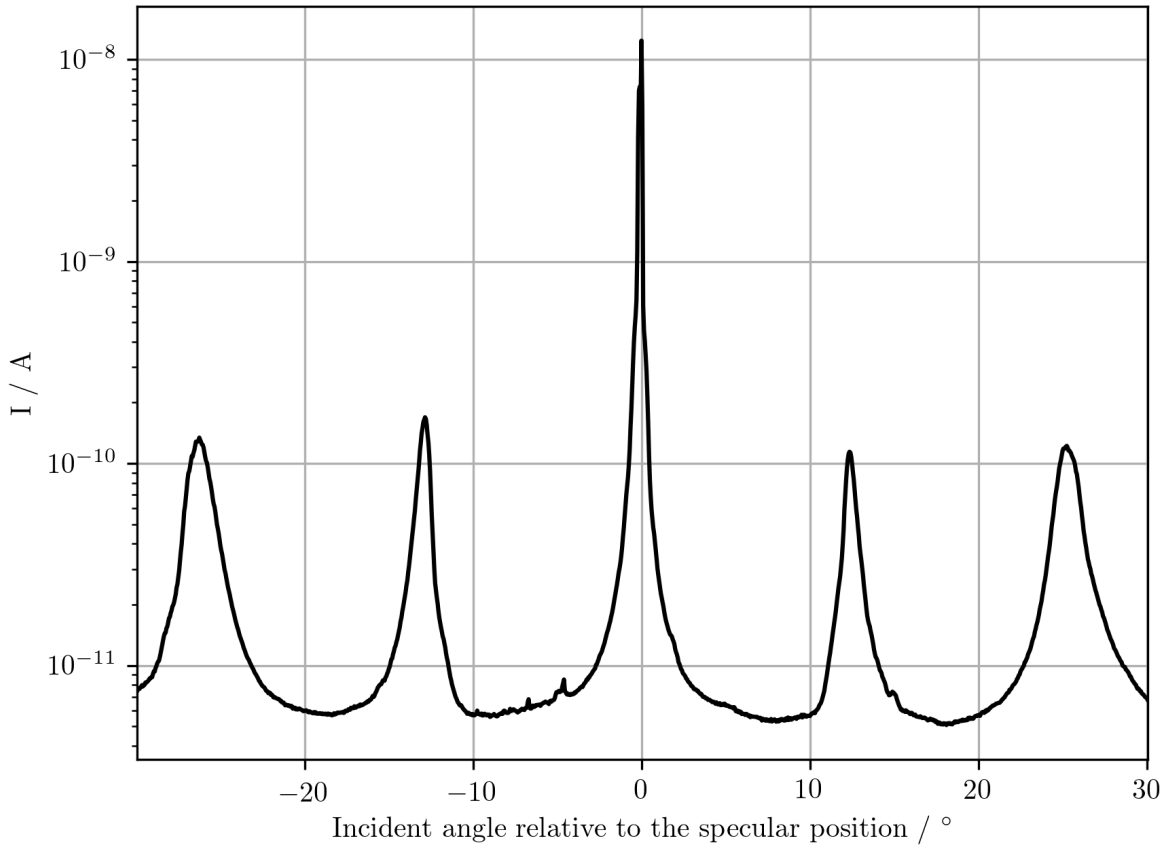


Figure A.3.: $\theta$-scan 3: Scattered Beam intensity versus angle of incidence $\theta$ of the measurement $N_\theta = 3$.

# Appendix B.

# Fitted peak data

Table B.1.: Fitted peak data 1: Fitting parameters of the peak area fit for the corresponding $\theta$-scan $N_\theta$ at the position $\theta$ using equation 5.5. The values starting with $\Delta$ indicate the corresponding errors.

| No. | $N_\theta$ | $\theta_0/^\circ$ | $\Delta\theta_0/^\circ$ | w$/^\circ$ | $\Delta w/^\circ$ | $\eta$ | $\Delta\eta$ |
|---|---|---|---|---|---|---|---|
| 0 | 0 | 43.945 | 0.005 | 0.74 | 0.01 | 0.89 | 0.03 |
| 1 | 0 | 22.217 | 0.001 | 0.076 | 0.003 | 1.0 | 0.1 |
| 2 | 0 | 0.155 | 0.006 | 0.78 | 0.01 | 0.74 | 0.05 |
| 3 | 1 | 49.2522 | 0.0007 | 0.537 | 0.001 | 0.600 | 0.007 |
| 4 | 1 | 22.1948 | 0.0004 | 0.0487 | 0.0006 | 0.18 | 0.05 |
| 5 | 1 | −4.975 | 0.002 | 0.433 | 0.003 | 0.63 | 0.02 |
| 6 | 2 | 53.9885 | 0.004 | 0.683 | 0.007 | 0.51 | 0.04 |
| 7 | 2 | 37.3996 | 0.0007 | 0.163 | 0.001 | 0.50 | 0.02 |
| 8 | 2 | 22.1730 | 0.0007 | 0.039 | 0.005 | 0.7 | 0.2 |
| 9 | 2 | 6.772 | 0.002 | 0.212 | 0.003 | 0.76 | 0.04 |
| 10 | 2 | −9.35 | 0.01 | 1.47 | 0.02 | 0.33 | 0.07 |
| 11 | 3 | 47.494 | 0.003 | 0.772 | 0.006 | 0.68 | 0.03 |
| 12 | 3 | 34.594 | 0.003 | 0.349 | 0.005 | 0.99 | 0.04 |
| 13 | 3 | 22.147 | 0.002 | 0.119 | 0.003 | 0 | 0.1 |
| 14 | 3 | 9.293 | 0.004 | 0.363 | 0.007 | 0.74 | 0.06 |
| 15 | 3 | −4.044 | 0.004 | 0.792 | 0.007 | 0.59 | 0.03 |

Table B.2.: Fitted peak data 2: Second part of the fitting parameters of the peak area fit for the corresponding $\theta$-scan $N_\theta$. The exact peak can be looked up in table B.1. The value $s$ is the one used in equation 5.5. $\Delta$s indicates the corresponding error.

| No. | $N_\theta$ | s | $\Delta s$ |
|---|---|---|---|
| 0 | 0 | 0.0266 | 0.0002 |
| 1 | 0 | 1.05 | 0.02 |
| 2 | 0 | 0.0342 | 0.0003 |
| 3 | 1 | 0.004 254 | 0.000 006 |
| 4 | 1 | 1.03 | 0.01 |
| 5 | 1 | 0.006 28 | 0.000 02 |
| 6 | 2 | 0.005 00 | 0.000 04 |
| 7 | 2 | 0.0373 | 0.002 |
| 8 | 2 | 1.4 | 0.1 |
| 9 | 2 | 0.0164 | 0.0002 |
| 10 | 2 | 0.000 186 | 0.000 003 |
| 11 | 3 | 0.009 56 | 0.000 05 |
| 12 | 3 | 0.008 89 | 0.000 08 |
| 13 | 3 | 0.75 | 0.02 |
| 14 | 3 | 0.0132 | 0.0002 |
| 15 | 3 | 0.010 19 | 0.000 07 |

Table B.3.: Calculated peak areas A and corresponding errors using equations 5.6 and 5.7. All areas are relative to the specular peak of the same spectrum and can be related to the peak parameters using No..

| No. | $N_\theta$ | A/% | $\Delta$A/% |
|---|---|---|---|
| 0 | 0 | 0.238 | 0.005 |
| 1 | 0 | 1.000 | 0.06 |
| 2 | 0 | 0.302 | 0.007 |
| 3 | 1 | 0.053 93 | 0.0002 |
| 4 | 1 | 1.000 | 0.03 |
| 5 | 1 | 0.0649 | 0.0006 |
| 6 | 2 | 0.059 | 0.001 |
| 7 | 2 | 0.105 | 0.001 |
| 8 | 2 | 1.00 | 0.2 |
| 9 | 2 | 0.066 | 0.002 |
| 10 | 2 | 0.0044 | 0.0001 |
| 11 | 3 | 0.109 | 0.001 |
| 12 | 3 | 0.051 | 0.001 |
| 13 | 3 | 1.000 | 0.06 |
| 14 | 3 | 0.072 | 0.002 |
| 15 | 3 | 0.115 | 0.002 |

# Bibliography


1. Toennies, J. P. Helium atom scattering: a gentle and uniquely sensitive probe of surface structure and dynamics. *Journal of Physics: Condensed Matter* **5,** A25 (1993).
2. Cabrera, N., Celli, V., Goodman, F. & Manson, R. Scattering of atoms by solid surfaces. I. *Surface Science* **19,** 67–92. ISSN: 0039-6028 (1970).
3. Konrad Kopitzki, P. H. *Einführung in die Festkörperphysik* 7. Auflage. ISBN: 9783662535783 (2017).
4. Tamtögl, A. *Surface Dynamics and Structure of Bi(111) from Helium Atom Scattering* PhD thesis (Graz University of Technology, 2012).
5. Lennard-Jones, J. & Devonshire, A. Diffraction and Selective Adsorption of Atoms at Crystal Surfaces. *Nature* **137,** 1069–1070 (1936).
6. Frisch, R. & Stern, O. Anomalien bei der spiegelnden Reflexion und Beugung von Molekularstrahlen an Kristallspaltflächen. I. *Zeitschrift für Physik* **84,** 430–442. ISSN: 0044-3328 (July 1933).
7. Knowling, J. R. B. *Helium atom scattering: experiment and the interpretation of experiment* PhD thesis (University of Cambridge, 2000).
8. Doak, R. B. *Measurement of surface phonon dispersion relations for LiF, NaF, and KCL through energy-analyzed inelastic scattering of a helium atomic beam* PhD thesis (Massachusetts Institute of Technology, 1981).
9. Lee, G. Y. H. *Resonant scattering of helium atoms from corrugated surfaces* PhD thesis (University of Cambridge, 2004).
10. Sanz, A. & Miret-Artés, S. Selective adsorption resonances: Quantum and stochastic approaches. *Physics Reports* **451,** 37–154. ISSN: 0370-1573 (2007).

11. Jardine, A., Hedgeland, H., Alexandrowicz, G., Allison, W. & Ellis, J. Helium-3 spin-echo: Principles and application to dynamics at surfaces. *Progress in Surface Science* **84,** 323–379. ISSN: 0079-6816 (2009).

12. Kraus, P. *et al.* A comparative study of the He–Sb(111) interaction potential from close-coupling calculations and helium atom scattering experiments. *Surface Science* **630,** 208–215. ISSN: 0039-6028 (2014).

13. *Topological Insulators* Volume 6 (ed Marcel Franz, L. M.) ISBN: 978-0-444-63314-9 (2013).

14. *Topological Insulators* (eds Frank Ortmann, S. R. & Valenzuela, S. O.) ISBN: 978-3-527-68158-7 (2015).

15. Schäpers, T. *Semiconductor Spintronics* ISBN: 978-3-11-036167-4 (2016).

16. Bessas, D. *et al.* Lattice dynamics in $Bi_2Te_3$ and $Sb_2Te_3$: Te and Sb density of phonon states. *Physical Review B* **86,** 224301 (22 Dec. 2012).

17. Dworski, S. *Atom Optical Methods for Surface Studies* PhD thesis (University of Cambridge, 2003).

18. Tamtögl, A. *et al.* Electron-phonon coupling and surface Debye temperature of $\mathbf{Bi_2Te_3}$(111) from helium atom scattering. *Physical Review B* **95,** 195401 (19 May 2017).

19. Hulpke, E. *Helium Atom Scattering from Surfaces* ISBN: 978-3-642-08115-6 (Springer-Verlag Berlin Heidelberg, 1992).

20. Farias, D. & Rieder, K.-H. Atomic beam diffraction from solid surfaces. *Reports on Progress in Physics* **61,** 1575 (1998).

21. Celli, V., Garcia, N. & Hutchison, J. Interpretation of selective adsorption in atom-surface scattering. *Surface Science* **87,** 112–128. ISSN: 0039-6028 (1979).

22. Lilienkamp, G. & Toennies, J. P. The observation of one-phonon assisted selective desorption and adsorption of He atoms in defined vibrational levels on a LiF (001) single crystal surface. *The Journal of Chemical Physics* **78,** 5210–5224 (1983).

23. Kraus, P. *et al.* Surface Structure of Bi(111) from Helium Atom Scattering Measurements. Inelastic Close-Coupling Formalism. *The Journal of Physical Chemistry C* **119.** PMID: 26257838, 17235–17242 (2015).

24. Boato, G., Cantini, P., Guidi, C., Tatarek, R. & Felcher, G. P. Bound-state resonances and interaction potential of helium scattered by graphite (0001). *Physical Review B* **20,** 3957–3969 (10 Nov. 1979).

# Acknowledgements

First of all, I would like to thank my supervisor Univ.-Prof. Dr. Wolfgang E. Ernst for his support and patience throughout this project. Without him, this work would not have been possible. I also want to thank Prof. Salvador Miret-Artés for his constant support and his expert advice on theory related problems. Moreover, I want to thank both of them for the great opportunity to visit Madrid, learn more about scattering theory and experience academic research abroad. Furthermore, I want to thank all my colleagues in Graz and Madrid, who made my work much more enjoyable and always had time to enlighten me with some technical discussion. Especially Patrick Kraus also guided me through the tough parts of the theory and provided me with tools used in the analysis, which made work a lot easier. I also gratefully acknowledge the help of Anton Tamtögl who produced the experimental data, read and corrected this work and answered a lot of my questions. Finally, I want to thank my family for their never ending support, particularly my girlfriend Monika who also help by reading and correcting this work.